Highlights

PEM Water Electrolyzer Robust Control Under Renewable Energy Source Intermittency

Meziane Ait Ziane, Michel Zasadzinski, Hugues Rafaralahy, Melika Hinaje, Marie-Cécile Péra

- Several PEMWE identification methods are proposed and discussed.
- The designed controller ensures robustness against RES variations.
- The proposed controller reduction method allows to achieve the same performance as the full-order controller in closed-loop.
- Experimental validation of PEMWE control under renewable energy source intermittency

PEM Water Electrolyzer Robust Control Under Renewable Energy Source Intermittency

Meziane Ait Ziane[a], Michel Zasadzinski[b], Hugues Rafaralahy[b], Melika Hinaje[c], Marie-Cécile Péra[d]

[a]*Group of Research in Electrical Engineering of Nancy (GREEN), Université de Lorraine, Nancy, 54000, France*
[b]*Research Center for Automatic Control of Nancy (CRAN), UMR CNRS 7039, Université de Lorraine, Nancy, 54000, France*
[c]*Laboratoire Réactions et Génie des Procédés (LRGP), CNRS, Université de Lorraine, Nancy, 54000, France*
[d]*FEMTO-ST Instiute, FCLAB, Université Marie et Louis Pasteur, CNRS, rue Thierry-Mieg, Belfort, 90010, France*

Abstract

This paper investigates the design and experimental validation of robust control for a proton exchange membrane water electrolyzer integrated with a stacked interleaved buck converter, aimed at regulating hydrogen production from renewable energy source. A model of the electrolyzer is obtained using the output error identification method. A State-space model of the electrolyzer coupled with the converter is therefore determined using the averaging method. To address variations in operating conditions during hydrogen production under renewable energy source intermittency, a robust control strategy based on normalized coprime factorizations is implemented. The obtained the full-order controller is reduced using a method that incorporates closed-loop behavior into the truncation process via frequency-weighted closed-loop sensitivity functions. Experimental validation demonstrates the controller's efficacy in adapting to changes in set-points and environmental conditions, underlining its theoretical robustness against renewable energy source intermittency.

Keywords: PEM water electrolyzer, hydrogen production, renewable energy source intermittency, robust control, normalized coprime factorizations, controller reduction.

1. Introduction

Reducing greenhouse gas emissions is a challenging goal, for which many efforts are being made in order to achieve carbon neutrality by 2050. One of the main strategies adopted in recent years has been to reduce dependency on fossil fuels and switch to green energies. Surplus energy from renewable sources needs to be stored to meet energy demand as required. One of the most attractive strategies is to store this energy as a hydrogen carrier. This hydrogen can be produced by a water electrolyzer that does not emit greenhouse gases. The hydrogen produced can then be used for various purposes: industry, transport, stationary.

Hydrogen can be produced by electrolysis of water using three principal technologies. Alkaline electrolyzer technology is the predominant solution for large-scale applications, as it is the technology with the greatest maturity [1].

Nevertheless, this technology has two major drawbacks: it operates in a low current range, around 0.5 A/cm^2, so the hydrogen flow rate per unit area is lower than with other technologies, and can hardly tolerate the variations of the energy supplied by a Renewable Energy Source (RES). Therefore, alkaline electrolysis is not suitable for the intermittency of RES. Proton Exchange Membrane Water Electrolysis (PEMWE) technology offers the advantage of operating under the intermittent effects of renewable energies and high current densities, up to 2 A/cm^2. The disadvantage of this technology is the high cost of the assembly electrode membrane, which uses rare metals [2]. Anion exchange membrane water electrolysis technology incorporates the advantages and disadvantages of both technologies: the maximum current density being of the order of 1 A/cm^2, although it is not yet mature for industrial applications and needs further developments [3].

As the present study focuses on green hydrogen production, taking into account the intermittency of RES is a key point. So the PEMWE technology has been retained and a robust control approach can be implemented to ensure the hydrogen production under uncertain conditions characterized by the intermittency of RES. The impact of the intermittency considered in this work concerns the fluctuations of the current leading to fluctuations of the hydrogen production. The designed controller must be robust against this intermittency, ensuring the desired hydrogen flow when the RES voltage varies.

In this paper, the $\mathcal{H}_\infty$ normalized coprime factorization method for controller design proposed in [4, 5, 6] is adopted as this approach translates the framework of real uncertainties into robustness constraints on a given nominal system.

The outline of this paper is presented below. In Section 2, a literature review is conducted on PEMWE control in a RES framework. The identification of the PEMWE electrical behavior model is addressed in Section 3. After describing the operating principles of PEMWE in Section 3.1, the Electrochemical Impedance Spectroscopy (EIS) and the Output Error (OE) approaches are used to obtain a transfer function from the current to the voltage of the PEMWE in Section 3.2. The coupling between the DC/DC converter with the obtained PEMWE model is provided in Section 3.3. The full-order controller design using the normalized coprime factorization approach is developed in Section 4.1 with closed-loop robustness study for RES framework. Since this design method leads to high order controllers, a reduced-order controller approach is applied in Section 4.2 by taking into account closed-loop considerations in the truncation procedure by means of frequency weighting. The robustness of full- and reduced-order designed controllers is analyzed in Section 4.3. The experimental validation of the full and reduced orders controllers is presented in Section 5. The controllers robustness against changes in nominal electrical operating conditions is addressed in Section 5.2, while robustness to the intermittency of RES framework is treated in Section 5.3. Discussions on the theoretical developments and experimental validations made in Sections 3, 4 and 5, conclusions and perspectives are

provided in Section 6.

2. Literature review on PEMWE in RES context

The PEMWE system is complex due to the interactions of electrochemical, electrical and thermal phenomena. Modeling such a system is a difficult task.

Some works have used an electrical approach to model the PEMWE: some authors have considered only a resistive behavior for the PEMWE [7, 8], while others works have described the anode and the cathode as a resistor for the membrane and two parallel RC circuits to introduce dynamics in the behavior [9, 10, 11]. A survey for the electrical modeling approach is presented in [12]. There are also other modeling methods for PEMWE systems such as bond graph modeling in [13] used in RES framework.

Maximizing PEMWE performances can be achieved by controling stack current: hydrogen production is proportional to current, so controlling current means controlling the desired hydrogen flow rate, which is not easy and challenging given the intermittent nature of the RES supplying the PEMWE [14].

The integration of PEMWE technology throughout the hydrogen production chain has been discussed in some papers. The authors in [15] highlight the complementary characteristics of solar and wind power make it possible to mitigate fluctuations in renewable energy generation and achieve higher utilisation rates for the PEMWE. An analysis of the optimisation of hydrogen production costs when using a PEMWE powered by renewable energy sources such as wind and solar power is given in [16]. The importance of developing control methods to optimise and ensure the performance of hydrogen production is emphasized [16]. A thermal management architecture for PEMWE that makes it flexible and reconfigurable when coupled with PV is proposed in [17]. The efficiency of the electrolyser exceeds 50% (see [17]), however it is suggested that the efficiency of the DC/DC converter be increased in order to improve the overall efficiency of the system. This can be achieved by designing a controller that takes into account variations in the energy supplied by the PV. Monitoring the system Balance of Plant (BOP), along with controlling the pressure and temperature of the PEMWE, allows to improve the efficiency of the system [18]. A machine learning-based model is proposed [19] to predict and estimate the current in the electrolyser. This model has been developed to analyze the behavior of PEMWE when integrated with RES.

As the PEMWE operates in Direct Current (DC) with low voltage and high current, AC/DC and DC/DC converters are required when the energy source is a wind turbine, while a DC/DC converter is needed when the source is a photovoltaic panel. Controlling the hydrogen flow rate means controlling the current from the DC/DC converter that is applied to the PEMWE. In the presence of RES intermittency and taking into account the dynamic behavior of the PEMWE, such a task is challenging [14].

The authors in [20] conduct a comparative analysis of different converter topologies suitable for hydrogen production using electrolyzers. This analysis includes the effect of electrolysis ageing and connection to AC and DC grids. The authors in [21] propose a DC/DC converter topology that guarantees a high-step down conversion ratio and low output current ripple for hydrogen production. This proposed converter architecture is validated in steady-state system behavior with a hardward in the loop. A Stacked Interleaved Buck Converter (SIBC) with four parallel phases is used in [11]: the advantage of this converter topology being that it cancels output current ripple and operates under fault conditions. The converter is validated experimentally in static operation, considering the PEMWE model as an RC circuit. The voltage of the PEMWE is controlled using an interleaved buck converter with a sliding-mode controller [22]. The same control objective is retained in [23], where a PI controller is employed and validated in simulation by using a converter based on a medium-voltage DC bus. A SIBC is used to control the current and voltage of the PEMWE in [24]. A first-order PEMWE model is obtained by identification using the ARX method. The coupled SIBC and PEMWE system is controlled by a PI controller through experimentations.

In the case where the energy source feeding the DC/DC converter is provided by a photovoltaic system, a buck converter is used in [25] with two control strategies: the first consists of tracking the maximum power of the photovoltaic system, so in this case the PEMWE current is variable and not maintained at a fixed current value, while the second consists of controlling the PEMWE current without tracking the maximum power of the photovoltaic system. Two PI controllers are designed to validate the approach experimentally. A static PEMWE model consisting of four resistors is considered in [26] with an incremental conductance MPPT algorithm to control a photovoltaic power by acting on the buck converter. Simulation validation is carried out without taking PEMWE current control into consideration. The same approach is adopted in [27, 8] using a PI controller, and employing a fuzzy logic approach coupled with the MPPT algorithm associated with the so-called “Perturbe and Observe” technique in [28]. These methods are validated through simulations.

In the case where the energy source feeding the DC/DC converter is provided by a wind energy source, the authors in [29] used a robust PI controller to regulate the electrolyzer current via a buck converter. The method is experimentally validated for two voltage changes supplying the converter, but without taking into account the intermittency of RES.

In the existing literature, the control of green hydrogen production taking into account the intermittency of RES from a control point of view is not fully investigated for the following reasons. The majority of the papers cited above consider the static behavior of the PEMWE, which is clearly far from what should be done in practice, so the validation of most approaches is carried out by simulations, but not with genuine experiments on test benches. Furthermore, no evaluation of the controllers in the event of abrupt variations in the energy supplied to the DC/DC

converters is considered. In addition, the study of controller robustness in the context of such energy intermittency has not yet been addressed in the literature.

3. PEMWE Identification and System Modeling

3.1. Operating Principle of PEMWE

Electrolysis is an electrochemical reaction involving an electric potential that splits water molecules, producing oxygen and hydrogen. For PEMWE, at the anode compartment, water is split into oxygen, electrons and protons as follows

$$H_2O \rightarrow 2H^+ + \frac{1}{2}O_2 + 2e^-. \tag{1}$$

Protons are transported to the cathode compartment through a polymer membrane, while electrons are transported from the electrical circuit to form hydrogen as bellow

$$2H^+ + 2e^- \rightarrow H_2. \tag{2}$$

The minimum required voltage for water splitting in one cell at standard conditions can be calculated as follows

$$V_{\text{int}} = \frac{\Delta H}{n_e F} = 1.48\,\text{V} \tag{3}$$

where

- $\Delta H = 285.84\,\text{kJ mol}^{-1}$ is the change of enthalpy,
- $n_e = 2$ is the number of transfered electrons,
- $F = 96485\,\text{C mol}^{-1}$ is Faraday's constant.

The theoretical formula to calculate the hydrogen flow rate $\dot{m}_{H_2}$ in mol s^{-1} is given by

$$\dot{m}_{H_2} = \frac{N_c i}{2F}\eta_{H_2} \tag{4}$$

where N_c is the number of cell, i is the applied current and η_{H_2} is the Faraday's efficiency, usually taken as 0.98 [30].

The stack PEMWE potential operating v at conditions T, P and i, where T is the stack temperature (K) and P gases pressure (Pa) can be expressed as the sum of activation overpotential η_{act} (V), ohmic overpotential η_{ohm} (V) and

diffusion overpotential η_{diff} (V) and is given by

$$v = N_c(V_{\text{int}} + \eta_{\text{act}} + \eta_{\text{ohm}} + \eta_{\text{diff}}) \tag{5}$$

To analyze and investigate the behavior of the PEMWE system, a static characteristic between the applied current i and the PEMWE voltage v is used. This static characteristic is known as the polarization curve and provides information on the operating and degradation states of the PEMWE system.

The polarization curve of the 400 W PEMWE stack used in this study is shown in Fig. 1 and technical specifications are given in Table 1. The test bench used to obtain this polarization curve does not include a temperature management system for the water entering the stack. For this reason, a current of 41 A is applied for 40 min to heat the stack, thereby improving electrolyzer performance before collecting the polarization curve values. The temperature of the PEMWE has a significant impact on its performance: a high temperature of around 80 °C facilitates charge transfer and increases proton conductivity across the membrane, thus accelerating the kinetics of the electrochemical reaction [31].

Table 1: PEMWE stack technical specifications

Parameters	Values	Units
Rated power	400	W
Cell number N_c	3	×
Max current	50	A
Active area	50	cm^2

Since the polarization curve describes the static behavior of the PEMWE, a static model derived from this polarization curve is not suitable for a control approach, as our study focuses on the impact of RES intermittency supplying PEMWE. Therefore, it is important to identify a model with current i as input and voltage v as output that captures the dynamic behavior of the PEMWE in order to design a control law for RES context. This is the aim of the next section.

3.2. PEMWE Identification

The aim of PEMWE model identification is to obtain several linear models that relate the PEMWE current input i to the PEMWE output voltage v at several operating points, using both frequency and temporal domains approaches.

3.2.1. Frequency Domain Approach

Electrochemical systems are often characterized using Electrochemical Impedance Spectroscopy (EIS) [32, 33]. This approach has recently been applied to PEMWE systems in [34, 35].

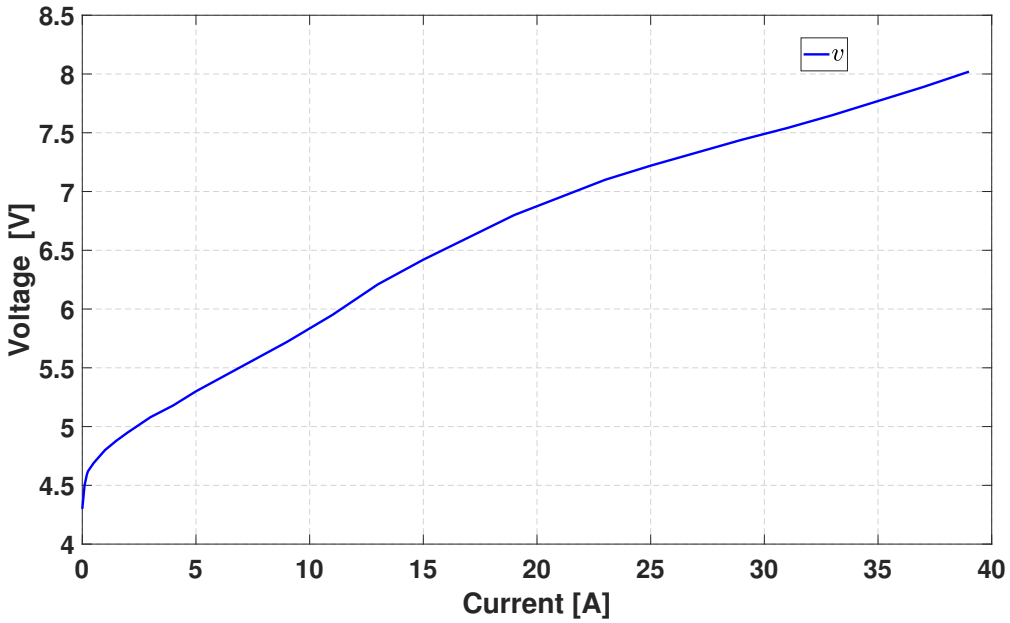

Figure 1: PEMWE polarization curve

In this paper, the galvanostatic approach is applied around an operating point of 15 A, with a frequency range spanning from 10 mHz to 10 kHz and an amplitude of 10% of the considered operating current point. Using "estimate transfer function" in Matlab (called tfest.m) some continuous time transfer functions are identified from the obtained frequency response data. The obtained frequency responses do not match with the experimental data for identified transfer functions of order 4 or less, whereas the obtained frequency responses are very close and match satisfactorily with the experimental data for identified transfer functions of order 5 or higher. The identified transfer functions of orders 5 and 6 are given by (6a) and (6b), respectively, where the red line Fig. 2 refers to the experimental data.

$$F_{EIS_5}(s) = \frac{0.02853s^5 + 205.5s^4 + 7.946.10^4 s^3 + 1.512.10^6 s^2 + 3.078.10^6 s + 6.377.10^5}{s^5 + 4611s^4 + 1.186.10^6 s^3 + 1.564.10^7 s^2 + 2.146.10^7 s + 2.979.10^6}, \tag{6a}$$

$$F_{EIS_6}(s) = \frac{0.02737s^6 + 403s^5 + 4.667.10^5 s^4 + 5.015.10^7 s^3 + 5.068.10^8 s^2 + 6.438.10^8 s + 1.009.10^8}{s^6 + 1.051.10^4 s^5 + 8.42.10^6 s^4 + 6.784.10^8 s^3 + 4.788.10^9 s^2 + 4.214.10^9 s + 4.684.10^8}, \tag{6b}$$

The Nyquist diagrams in Fig. 2 show that the two identified models are close and match well with experimental data.

The applied step responses plotted in Fig. 3 validate the identified models with the frequency approach.

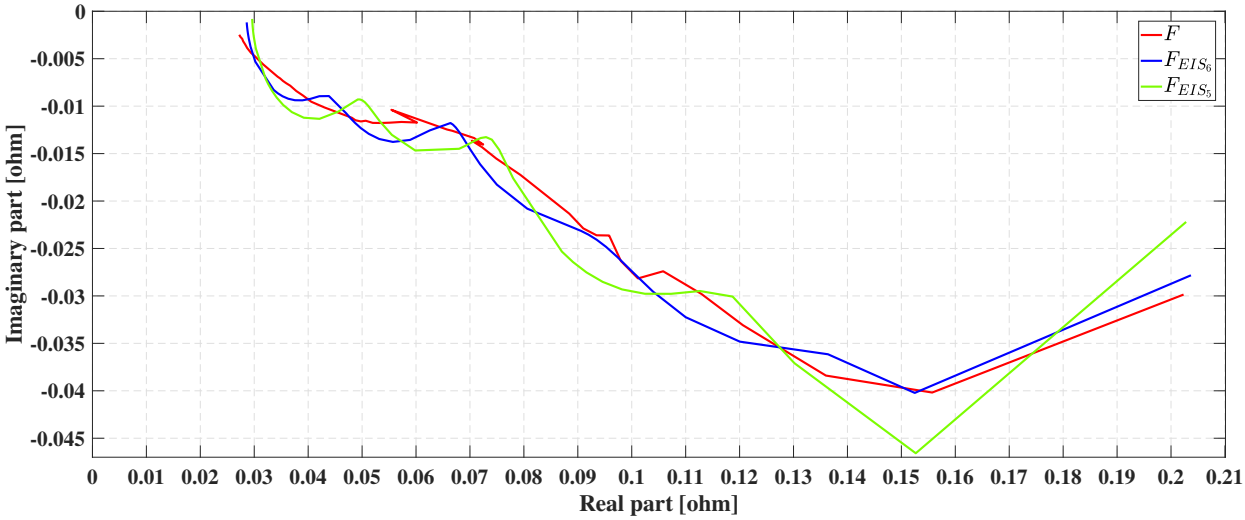

Figure 2: Nyquist diagrams for EIS approach

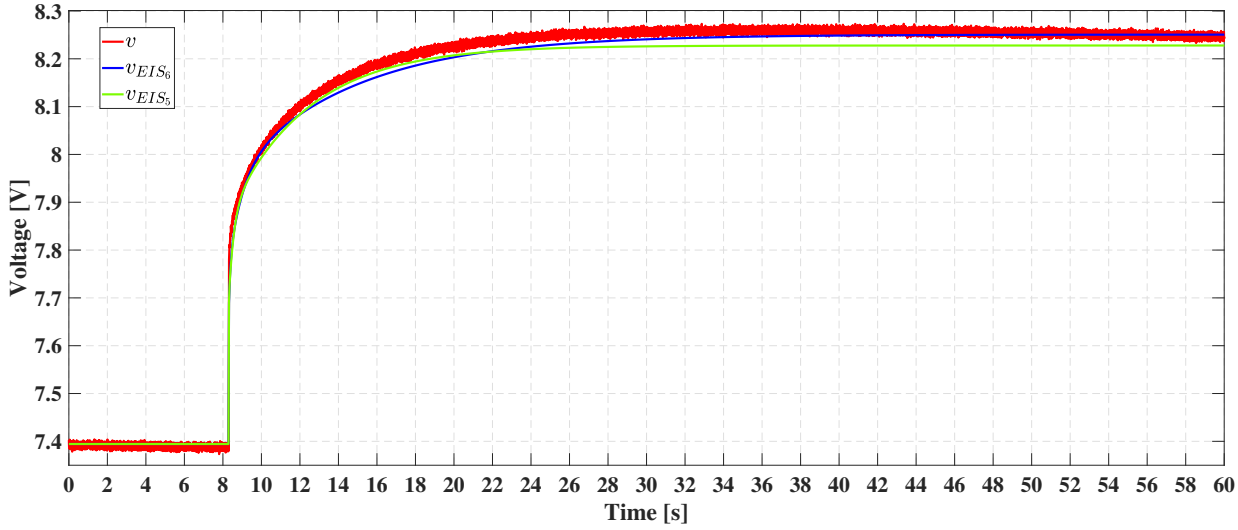

Figure 3: Step responses for validation for EIS approach

3.2.2. Temporal Domain Approach

Since the identification procedure provides linear models, the initial conditions for both current and voltage should be reset to zero. To do that, we define signals $\widetilde{i}_j$ and $\widetilde{v}_j$ as follows

$$\widetilde{i}_{j_k} = i_{j_k} - i_{j_0} \tag{7a}$$

$$\widetilde{v}_{j_k} = v_{j_k} - v_{j_0} \tag{7b}$$

where $\widetilde{i}_{j_k} = 0$ and $\widetilde{v}_{j_k} = 0$ when $k \leqslant 0$, k refers to the sample number at the time sample kT_s and j refers to the j^{th} operating point.

The estimation $\widehat{v}_j$ of $\widetilde{v}_j$ in discrete-time is expressed using a discrete-time transfer function $F_{d_j}(z)$ as follows

$$\widehat{V}_{d_j}(z) = F_{d_j}(z)\widetilde{I}_{d_j}(z) \tag{8}$$

where $\widehat{V}_{d_j}(z)$ and $\widetilde{I}_{d_j}(z)$ are the $\mathcal{Z}$ transforms of discrete-time signals $\widehat{v}_j$ and $\widetilde{i}_j$. The transfer function $F_{d_j}(z)$ in (8) is given by

$$F_{d_j}(z) = \frac{N_{d_j}(z)}{D_{d_j}(z)} = \frac{b_{j_{n-1}}z^{n-1} + \cdots + b_{j_1}z + b_{j_0}}{z^n + a_{j_{n-1}}z^{n-1} + \ldots + a_{j_1}z + a_{j_0}} \tag{9}$$

where $b_{j_{n-1}}, \ldots, b_{j_0}, a_{j_{n-1}}, \ldots a_{j_0}$ are the parameters to be identified, such that the estimation error ε_j defined as

$$\varepsilon_{j_k} = \widetilde{v}_{j_k} - \widehat{v}_{j_k} \tag{10}$$

is minimized using the Output-Error (OE) identification method proposed in textbooks [36, 37, 38]. Combining (8), (9) and (10), the PEMWE voltage output $\widetilde{v}_j$ at time instant k can be expressed by the following recurrence relation

$$\widetilde{v}_{j_k} = \sum_{h=0}^{n-1} b_{j_h}\widetilde{i}_{j_{k-n+h}} - \sum_{h=0}^{n-1} a_{j_h}\widetilde{v}_{j_{k-n+h}} + \varepsilon_{j_k} + \sum_{h=0}^{n} a_{j_h}\varepsilon_{j_{k-n+h}}. \tag{11}$$

which is used to minimize ε_j with the OE method.

The validation of the obtained models is made using the following decorrelation test proposed in [38]

$$R_{j_N}(\xi) = \frac{\sum_{k=\xi}^{N} \overline{\varepsilon}_{j_k}\widehat{v}_{j_{k-\xi}}}{\left(\sum_{k=1}^{N}\widehat{v}_{j_k}^2 \sum_{k=1}^{N}\overline{\varepsilon}_{j_k}^2\right)^{0.5}} \tag{12}$$

where $\overline{\varepsilon}_j$ is the zero-mean version of ε_j in (10), N is the number of measurement samples and $\xi = 0, 1, \ldots, n$, with $n = \deg(D_{d_j}(z))$. The identified model is considered valid if

$$\left|R_{j_N}(\xi)\right| \leqslant \ell_c = \frac{2.17}{\sqrt{N}} \quad \text{or} \quad \left|R_{j_N}(\xi)\right| \leqslant \ell_p = 0.15. \tag{13}$$

Three operating points, i.e. $j = 1, 2, 3$, are considered (see (7)):

- 1st operating point: $i_{1_0} = 8$ A and $v_{1_0} = 6.39$ V,
- 2nd operating point: $i_{2_0} = 10$ A and $v_{2_0} = 7.43$ V,
- 3rd operating point: $i_{3_0} = 14$ A and $v_{3_0} = 7.51$ V.

For the identification procedure the same Pseudo Random Binary Sequence (PRBS) excitation is applied to all considered operating points with a magnitude of 4 A, and a sampling period $T_s = 0.001$ s. The PRBS signal used for the 1st operating point is shown in Fig. 4. For the 2nd and 3rd operating points, only the current range is changed: 10 A to 14 A and 14 A to 18 A, respectively.

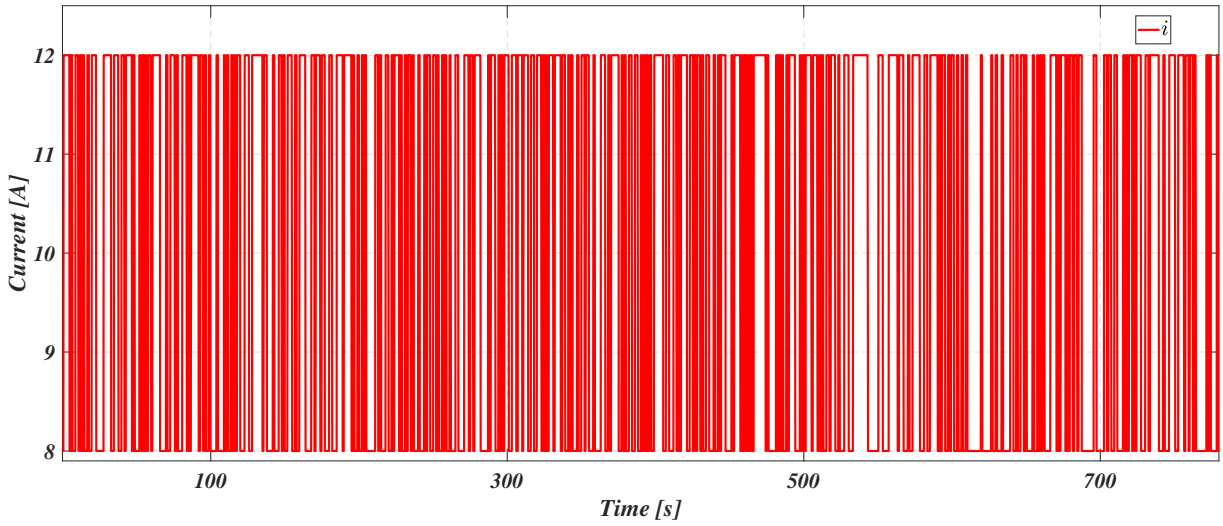

Figure 4: PRBS current for 1st operating point

Applying the OE identification methods to the three operating points ($j = 1, 2, 3$) with Identification Matlab Toolbox [39] yields the corresponding estimated voltages v_{OE_j}. For each operating point, the models that satisfy the decorrelation test in (12) and (13) with least order are given by

$$F_{OE_1}(z) = \frac{0.04943z^4 - 0.1467z^3 + 0.1451z^2 - 0.04784z}{z^4 - 3.25z^3 + 3.768z^2 - 1.786z + 0.2682}, \tag{14a}$$

$$F_{OE_2}(z) = \frac{0.02767z^2 - 0.02767z}{z^2 - 1.596z + 0.5963}, \tag{14b}$$

$$F_{OE_3}(z) = \frac{0.06052z^2 + 2.665 \times 10^{-7}z - 0.06049}{z^2 - 0.0001013z - 0.9996}. \tag{14c}$$

where the decorrelation test is given in Table 2.

Fig. 5 shows the measured voltage v_1 compared with the estimated voltage $v_{OE1} = \widehat{v_1} + v_{1_0}$ for the 1st operating point where $v_{1_0} = 6.39$ V.

Table 2: Decorrelation test in (12) and (13)

ξ	1	2	3	4
R_{1_N}	0.016158	0.0158	0.015324	0.015061
R_{2_N}	0.048888	0.048961	×	×
R_{3_N}	0.1194	0.11199	×	×

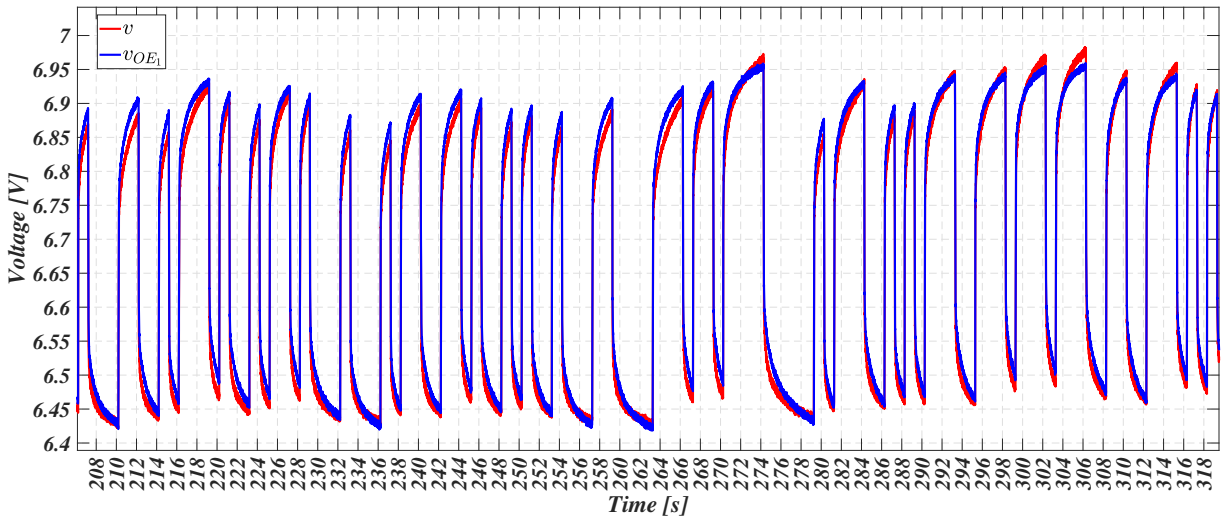

Figure 5: Measured and estimated voltages v and v_{OE_1} for 1st operating point

Remark 1. It is important to note that voltages v_{j_0} include the minimum required voltage for water splitting $V_{\text{int}} = N_c \times 1.48\,\text{V}$ defined in (3). □

3.2.3. Model Selection

Let $F^c_{OE_1}(s)$, $F^c_{OE_2}(s)$ and $F^c_{OE_3}(s)$ be continuous time models obtained by applying the bilinear transform to the discrete time models $F_{OE_1}(z)$, $F_{OE_2}(z)$ and $F_{OE_3}(z)$, respectively. In Fig. 6, the Nyquist diagrams are plotted for the three identified systems $F^c_{OE_1}(s)$, $F^c_{OE_2}(s)$ and $F^c_{OE_3}(s)$. The red curve in Fig. 2 and in Fig. 6 are identical.

In Fig. 6, the Nyquist diagram obtained from $F^c_{OE_1}(s)$ is closer to the Nyquist diagram given by experimental data than one generated by $F^c_{OE_2}(s)$ and $F^c_{OE_3}(s)$. However, the Nyquist diagrams obtained from $F_{EIS_5}(s)$ and $F_{EIS_6}(s)$ plotted in Fig. 2 match the experimental data much better than the one obtained with $F^c_{OE_1}(s)$.

In Fig. 2 to Fig. 3, the responses obtained with $F_{EIS_6}(s)$ are closer to the experimental data that the responses generated with $F_{EIS_5}(s)$. The $F_{EIS_6}(s)$ model is thus chosen for control law design in Section 4.

Since the system to be controlled is the PEMWE coupled with a Stacked Interleaved Buck Converter (SIBC) which is composed by electrical components, it is useful to describe the obtained transfer function $F_{EIS_6}(s)$ with an equivalent electrical circuit. This approach facilitates the formulation of ordinary differential equations that describe the behavior of the entire system (PEMWE + SIBC).

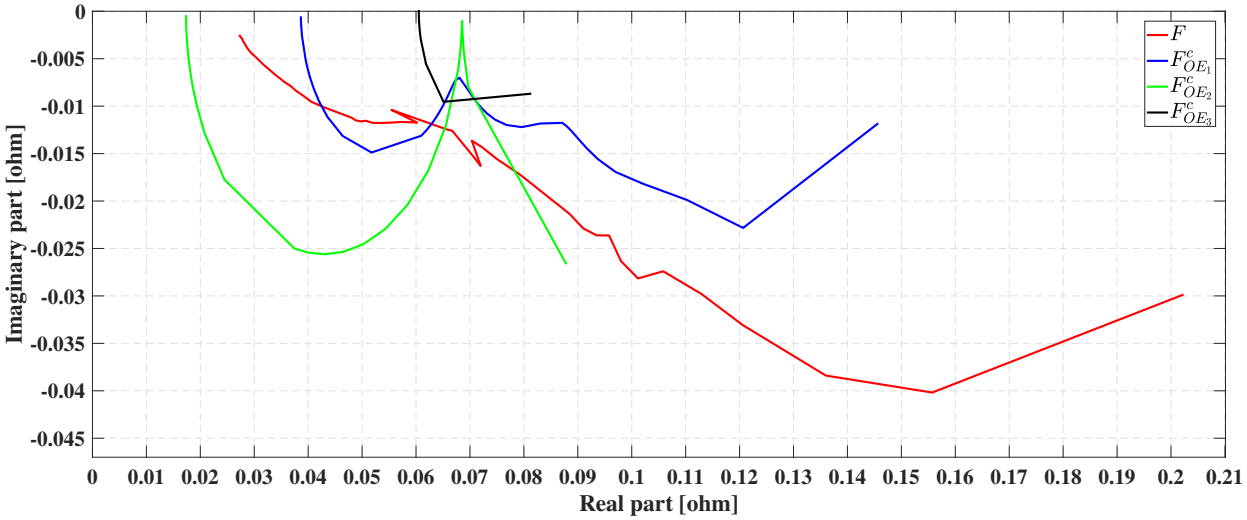

Figure 6: Nyquist diagrams for temporal approach

Using residue theorem, also known as partial fraction decomposition for Laplace transforms [40], $F_{EIS_6}(s)$ in (6b) can be written as

$$F_{EIS_6}(s) = \sum_{h=1}^{6} \frac{R_h}{C_h R_h s + 1} + R_0, \tag{15}$$

where

$$R_6 = 100.06\,\Omega,\ R_5 = 13.588\,\Omega,\ R_4 = 1.4068\,\Omega,$$

$$R_3 = 0.20564\,\Omega,\ R_2 = 0.040826\,\Omega,\ R_1 = 0.0085339\,\Omega,$$

$$C_6 = 1.0361 \times 10^{-6}\,\text{F},\ C_5 = 9.4843 \times 10^{-5}\,\text{F},\ C_4 = 0.0086629\,\text{F},$$

$$C_3 = 0.72622\,\text{F},\ C_2 = 27.953\,\text{F},\ C_1 = 901.43\,\text{F},$$

$$R_0 = 0.027366\,\Omega.$$

The equivalent electrical circuit of the obtained PEMWE model is given in Fig 7.

It is important to note that the electrical parameters of the obtained equivalent electrical circuit in Fig. 7 do not have physical significance because they are obtained after the identification procedure. So these parameters do not describe the stoichiometric reactions at the anode, cathode and resistive membrane as can be found in the literature [12].

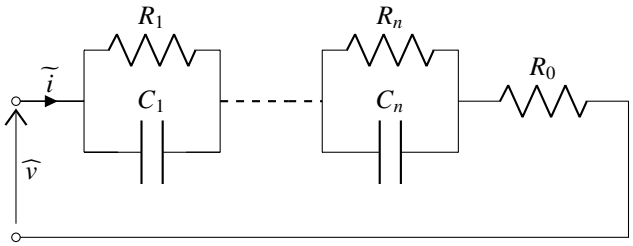

Figure 7: PEMWE equivalent electrical circuit for $F_{EIS_6}(s)$ with $n = 6$

3.3. Modeling of PEMWE with SIBC

The DC/DC converter used in the test bench shown in Fig. 16 in Section 5 is a SIBC studied in [41]. The whole system composed of the PEMWE coupled with a SIBC is illustrated in Fig. 8 where the PEMWE equivalent electrical circuit from Fig. 7 is used for modeling purposes instead of the actual electrolyzer. The nominal values of the electrical components are: $L_p = L_s = 426 \times 10^{-6}$ H, $R_{\ell_p} = R_{\ell_s} = 0.06\,\Omega$, $C_p = 10^{-4}$ F and $C_s = 10^{-5}$ F.

V_i in Fig. 8 is the voltage of the RES that supplies the SIBC coupling with the PEMWE. The SIBC is composed from two circuits in parallel (primary (with index p) and secondary (with index s) circuits). These two circuits are controlled oppositely by two pairs of insulated-gate bipolar transistors ($\mathcal{T}_1, \mathcal{T}_4$) during the duty cycle $(1 - D)T_{\text{pwm}}$ and ($\mathcal{T}_2, \mathcal{T}_3$) during the duty cycle DT_{pwm} where D is a percentage of the period $T_{\text{pwm}} = 5 \times 10^{-5}$ s of the Pulse Modular Generator (PWM).

The state vector x and the measurements y are given by

$$x^T = \begin{bmatrix} i_p & i_s & \widehat{v} & v_{c_s} & v_{c_1} & \dots & v_{c_n} \end{bmatrix} \tag{16a}$$

$$y^T = \begin{bmatrix} \widetilde{i} & \widehat{v} \end{bmatrix} \tag{16b}$$

Applying the Kirchhoff's laws to the circuit in Fig. 8 during DT_{pwm} yields

$$
\begin{aligned}
L_p \dot{i}_p &= V_i - \widehat{v} - R_{\ell_p}\, i_p \\
L_s \dot{i}_s &= -v_{c_s} - \widehat{v} - R_{\ell_s}\, i_s \\
C_p \dot{\widehat{v}} &= i_p + i_s - \frac{\widehat{v}}{R_0} + \sum_{h=1}^{n} \frac{v_{c_h}}{R_0} \\
C_s \dot{v}_{c_s} &= i_s \\
\dot{v}_{c_1} &= \frac{-v_{c_1}}{R_1 C_1} + \frac{\widehat{v} - \sum_{h=1}^{n} v_{c_h}}{C_1 R_0} \\
&\vdots \\
\dot{v}_{c_n} &= \frac{-v_{c_n}}{R_n C_n} + \frac{\widehat{v} - \sum_{h=1}^{n} v_{c_h}}{C_n R_0} \\
R_0 \widetilde{i} &= \widehat{v} - \sum_{h=1}^{n} v_{c_h}
\end{aligned}
$$

and the primary circuit is associated with the following state-space realization

$$\dot{x} = A_1 x + B_1 V_i \tag{17a}$$

$$y = C_1 x \tag{17b}$$

Applying the Kirchhoff's laws to the circuit in Fig. 8 during $(1-D)T_{\text{pwm}}$ yields

$$
\begin{aligned}
L_p \dot{i}_p &= -\widehat{v} - R_{\ell_p}\, i_p \\
L_s \dot{i}_s &= V_i - v_{c_s} - \widehat{v} - R_{\ell_s}\, i_s \\
C_p \dot{\widehat{v}} &= i_p + i_s - \frac{\widehat{v}}{R_0} + \sum_{h=1}^{n} \frac{v_{c_h}}{R_0} \\
C_s \dot{v}_{c_s} &= i_s \\
\dot{v}_{c_1} &= \frac{-v_{c_1}}{R_1 C_1} + \frac{\widehat{v} - \sum_{h=1}^{n} v_{c_h}}{C_1 R_0} \\
&\vdots \\
\dot{v}_{c_n} &= \frac{-v_{c_n}}{R_n C_n} + \frac{\widehat{v} - \sum_{h=1}^{n} v_{c_h}}{C_n R_0} \\
R_0 \widetilde{i} &= \widehat{v} - \sum_{h=1}^{n} v_{c_h}
\end{aligned}
$$

and the secondary one corresponds to the following state-space realization

$$\dot{x} = A_2 x + B_2 V_i \tag{18a}$$

$$y = C_2 x \tag{18b}$$

The matrices of the two state-space realizations are given by

$$A_1 = A_2 = \begin{bmatrix} \frac{-R_{\ell_p}}{L_p} & 0 & \frac{-1}{L_p} & 0 & 0_{1\times n} \\ 0 & \frac{-R_{\ell_s}}{L_s} & \frac{-1}{L_s} & \frac{-1}{L_s} & 0_{1\times n} \\ \frac{1}{C_p} & \frac{1}{C_p} & \frac{-1}{R_0 C_p} & 0 & \frac{1_{1\times n}}{R_0 C_p} \\ 0 & \frac{1}{C_s} & 0 & 0 & 0_{1\times n} \\ 0_{n\times 1} & 0_{n\times 1} & \mathcal{A}_0 & 0_{n\times 1} & \mathcal{A} \end{bmatrix}$$

$$B_1 = \begin{bmatrix} \frac{1}{L_p} \\ 0_{(3+n)\times 1} \end{bmatrix}, \quad B_2 = \begin{bmatrix} 0 \\ \frac{1}{L_s} \\ 0_{(2+n)\times 1} \end{bmatrix}$$

$$C_1 = C_2 = \begin{bmatrix} 0 & 0 & \frac{1}{R_0} & 0 & \frac{-1_{1\times n}}{R_0} \\ 0 & 0 & 1 & 0 & 0_{1\times n} \end{bmatrix}$$

where $\mathcal{A} \in \mathbb{R}^{n\times n}$ and $\mathcal{A}_0 \in \mathbb{R}^{n\times 1}$ are given by (for $h = 1, \ldots, n$ and $q = 1, \ldots, n$)

$$\begin{aligned} \mathcal{A}(h,h) &= \frac{-1}{R_h C_h} + \frac{-1}{R_0 C_h}, \\ \mathcal{A}(h,q) &= \frac{-1}{R_0 C_h} \qquad h \neq q, \\ \mathcal{A}_0(h) &= \frac{1}{R_0 C_h}. \end{aligned}$$

The dynamic behavior of the whole system shown in Fig. 8 can be described by the switching between the primary (during DT_{pwm}) and secondary (during $(1-D)T_{\text{pwm}}$) circuits.

To design a unified control law associates to the switching system given by (17) and (18), Middlebroock and Cuk developed a state-space averaging method in [42] that provides a unified linear system (for further explanations on state-space averaging approach, the readers can refer to [43]). For the systems (17) and (18), the resulting averaging model is given by

$$\dot{x} = Ax + Bu \tag{19a}$$

$$y = Cx \tag{19b}$$

where $A = A_1 = A_2$, $C = C_1 = C_2$ and matrix B is given by

$$B = (B_1 - B_2)V_i \tag{20}$$

and the control u is an input of PWM in Fig. 8 representing the duty cycle associated to the switching between the primary and secondary circuits.

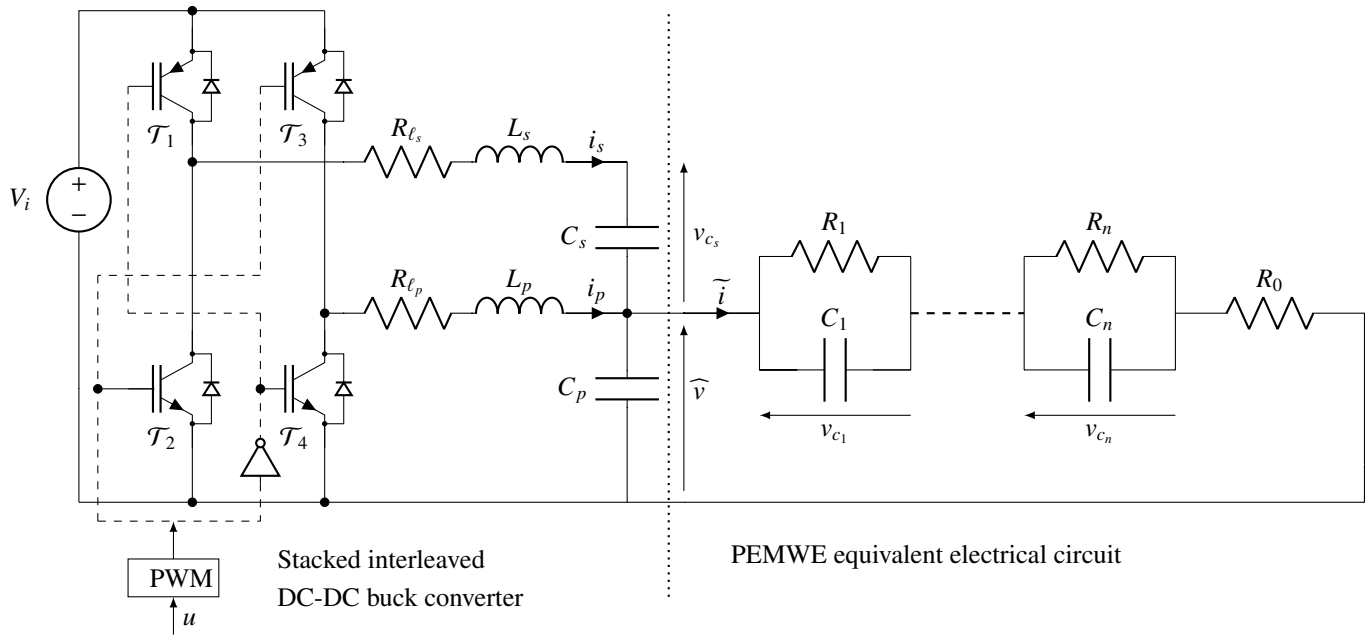

Figure 8: Stacked interleaved DC-DC buck converter with pulse width modulation (PWM) and electrical model of PEMWE

Then the transfer function of the system described by (19) is given by $G(s)$ where

$$G(s) = C\,(sI_{4+n} - A)^{-1}\,B \tag{21}$$

where $4 + n$ is the length of the state vector x given in (16a). In Eqs (16) to (21) and in Fig. 7 and Fig. 8, n is the order of the PEMWE identified model. Since the PEMWE model given by $F_{EIS_6}(s)$ is selected for the design of the robust $\mathcal{H}_\infty$ control law, we get $n = 6$ in (21) where the resistors and capacitors in (16) to (20) are given in (15).

4. Robust $\mathcal{H}_\infty$ Control Design

4.1. Full-Order 2-DOF Controller Design

4.1.1. Controller Design Specifications

In a RES framework, the main issue is that the energy supplied to the SIBC and PEMWE varies due to their intermittency. These variations are represented by V_i in the state-space model given in (19). From the control point

of view, the variations of V_i can be seen as a parameter uncertainty. In this paper, the nominal value of V_i is 40 V. As mentioned in the Introduction section, the range of V_i variations guarantees the desired hydrogen production, i.e. allows the electrolyzer current i to be maintained around a desired operating point.

The controller is designed in order to guarantee a desired hydrogen flow rate independently of the uncertainties due to variations of V_i in RES framework. As mentioned in Section 3.1, the hydrogen flow rate is strongly related to the current i as shown in (4). For this reason an integral action is required to control the current i at a desired operating point. It should be noted that the voltage v is a useful indicator of the operating state of the PEMWE system as shown in (5). So it is interesting to employ this second available measurement in the controller design.

The $\mathcal{H}_\infty$ loop-shaping approach based on normalized coprime factorization and described in [4], [5], [6] is a controller design framework well adapted to take into account the design specifications described in previous paragraph, associated to robustness considerations.

This loop-shaping approach is based on the closed-loop structure given in Fig. 9.

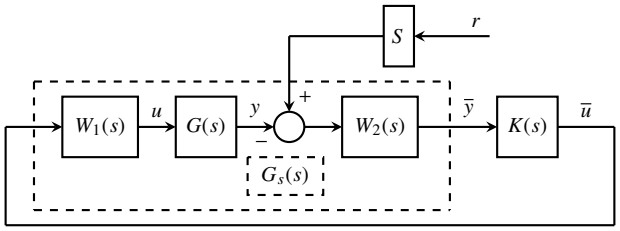

Figure 9: Closed-loop structure for loop-shaping controller design

In Fig. 9, $G_s(s)$ is shaped plant given by

$$G_s(s) = W_2(s)G(s)W_1(s) \tag{22}$$

where $W_1(s)$ and $W_2(s)$ are weightings to be determined in order to satisfy the design specifications. $K(s)$ is the controller calculated using $G_s(s)$, but the controller to be implemented is $\mathcal{K}(s)$ given by

$$\mathcal{K}(s) = W_1(s)K(s)W_2(s). \tag{23}$$

In this design method, $\overline{u}$ and $\overline{y}$ are considered as pseudo-measurements and pseudo-control input, respectively, but the measurements and control input for the implemented controller $\mathcal{K}(s)$ are y and u, respectively. In addition, the operating set-point is represented by $S \times r$ with $S = \begin{bmatrix} 1 & 0 \end{bmatrix}^T$. The aim of the controller $K(s)$ is to minimize the

following criterion

$$\min_{K(s)\in\mathcal{H}_\infty} \underbrace{\left\| \begin{bmatrix} K(s) \\ I \end{bmatrix} (I + G_s(s)K(s))^{-1} \begin{bmatrix} I & G_s(s) \end{bmatrix} \right\|_\infty}_{(b(G_s(s),K(s)))^{-1}} \tag{24}$$

where $\mathcal{H}_\infty$ is the set of all transfer matrices that are stable and proper, i.e. the transfer matrix $L(s)$ belongs to $\mathcal{H}_\infty$ if and only if $L(s)$ is analytic for $\mathrm{Re}(s) \geqslant 0$ and $\lim_{s\to\infty} |L(s)|$ is bounded [44], [45]. If $L(s) \in \mathcal{H}_\infty$, the H-infinity norm of $L(s)$ is the maximal singular value of $L(s)$ (see [44], [45]) and is called $\|L(s)\|_\infty$.

If $b(G_s(s), K(s)) \leqslant \varepsilon_s$ than the designed controller $K(s)$ robustly stabilize all uncertain shaped plants $G_{s\Delta}(s)$ given by

$$G_{s\Delta}(s) = (M_s(s) + \Delta_{M_s}(s))^{-1}(N_s(s) + \Delta_{N_s}(s)), \tag{25}$$

where the pair $M_s(s) \in \mathcal{H}_\infty$ and $N_s(s) \in \mathcal{H}_\infty$ is a Normalized Left Coprime Factorization (NLCF) in $\mathcal{H}_\infty$ of $G_s(s)$, i.e.

$$G_s(s) = M_s^{-1}(s)N_s(s) \tag{26a}$$

$$I = M_s(s)M_s^T(-s) + N_s(s)N_s^T(-s), \quad \forall\, s \in \mathbb{C}. \tag{26b}$$

and where the coprime uncertainties are bounded as

$$\left\| \begin{bmatrix} \Delta_{M_s}(s) & \Delta_{N_s}(s) \end{bmatrix} \right\|_\infty < \varepsilon_s. \tag{27}$$

The state-space formula for NLCF is given in [46] and in lemma 2.1 in [4].

Since the robustness analysis is made with the implemented controller $\mathcal{K}(s)$ associated to the plant $G(s)$ (i.e. the criterion $b(G(s), \mathcal{K}(s))$) instead of with the computed controller $K(s)$ associated to the shaped plant $G_s(s)$ (i.e. the criterion $b(G_s(s), K(s))$), the following problem appears: the $\mathcal{H}_\infty$ norm of the sensitivity function $(I+G(s)\mathcal{K}(s))^{-1}G(s)$ will necessarily be greater than 50 dB (see the blue curve in Fig. 10) in the frequency range from 10 to 20 000 rad/s (high-frequency range), since the singular values of $G(s)$ are around 50 dB and the singular values of $(I+G(s)\mathcal{K}(s))^{-1}$ tend towards one in this frequency range.

Remark 2. A consequence of the above analysis is that $b(G(s), \mathcal{K}(s))$ cannot be used to evaluate the robustness and will be replaced by the modulus margin given by $\overline{b}(G(s), \mathcal{K}(s)) = \left\|(1 + \mathcal{K}(s)G(s))^{-1}\right\|_\infty^{-1}$. □

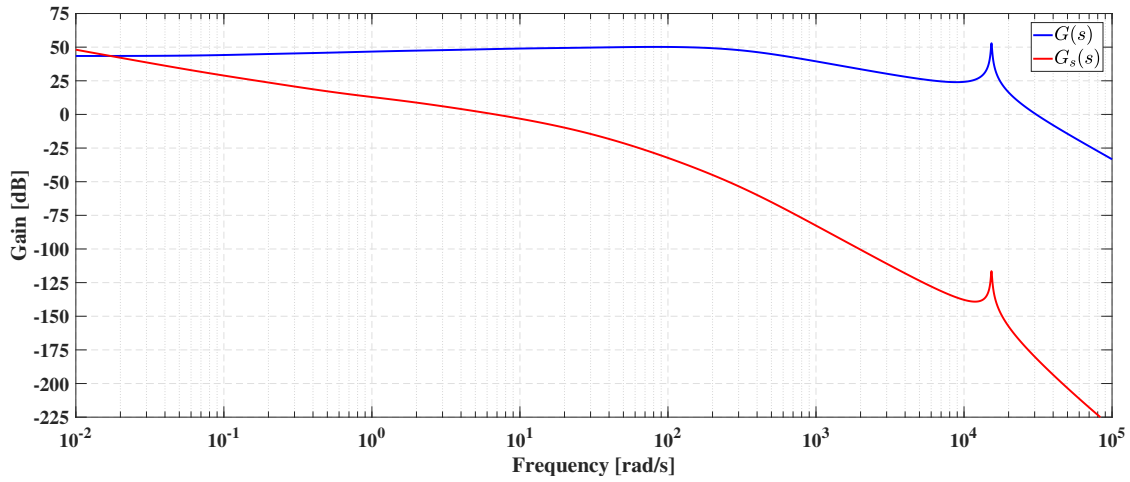

Figure 10: Frequency singular values of $G(s)$ and $G_s(s)$

This analysis leads to the following specifications on the shaped plant $G_s(s)$:

- determining the weighting $W_1(s)$ in order to reducing drastically the singular values of $G_s(s)$ at high frequency, with bandwidth approximately three decade before the peak on $G_s(s)$,
- determining the weighting $W_2(s)$ in order to introducing an integral action (at low frequency) between the reference r and the measurement current $\widetilde{i}$ with adding proportional actions based on the available measurements ($\widetilde{i}$ and $\widehat{v}$).

These specifications are achieved by choosing the weightings $W_1(s)$ and $W_2(s)$ as follows

$$W_1(s) = \frac{7.875 \times 10^{-6} s + 0.7875}{s^2 + 31.5s + 45}, \tag{28a}$$

$$W_2(s) = \begin{bmatrix} \frac{1}{s} & 0 \\ 1 & 0 \\ 0 & 1 \end{bmatrix}. \tag{28b}$$

The singular values of the obtained shaped plant $G_s(s)$ in (22) are plotted with the red curve in Fig. 10 and satisfy the design specifications.

The choice of $W_2(s)$ in (28b) allows to rewrite the structure of the closed-loop shown in Fig. 9 in the equivalent

2-DOF controller structure given in Fig. 11, where

$$\overline{y} = \begin{bmatrix} \overline{y}_1 & \overline{y}_2 & \widehat{v} \end{bmatrix}^T, \tag{29a}$$

$$K(s) = \begin{bmatrix} K_i(s) & K_{p_i}(s) & K_{p_v}(s) \end{bmatrix}. \tag{29b}$$

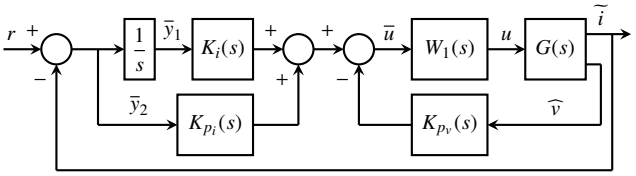

Figure 11: 2-DOF structure of the closed-loop

4.1.2. Full-Order Controller Design

The method proposed in [4], [5], [6] by McFarlane and Glover, gives a controller $K(s)$ that minimizes $b(G(s), K(s))$ in (24) where the singular values of $K(s)G_s(s)$ are as close as possible to those of $G_s(s)$. The controller $K(s)$ is synthesized in three steps given below.

a) Compute a state-space realization of the shaped plant $G_s(s)$ defined in (22): $G_s(s) = C_s(sI_{13} - A_s)^{-1}B_s$.

b) Compute the solutions X and Z of the two following algebraic Riccati equations

$$0 = A_s^T X + XA_s - XB_sB_s^T X + C_s^T C_s, \tag{30a}$$

$$0 = A_s Z + ZA_s^T - ZC_s^T C_s Z + B_s B_s^T. \tag{30b}$$

c) The state-space realization of controller $K(s)$ in (29b) is given by (see corollary 5.1 in [4] and in corollary 4.15 in [5])

$$K(s) = C_K(sI_{13} - A_K)^{-1}B_K \tag{31}$$

where

$$A_K = A_s - B_sB_s^T X - \mu^2 QZC_s^T C_s \tag{32a}$$

$$B_k = \mu^2 QZC_s^T \tag{32b}$$

$$C_K = B_s^T X \tag{32c}$$

and

$$\mu = \sqrt{1 + \rho\lambda_{\max}(ZX)}, \tag{33a}$$

$$\Psi = (I_{13} + ZX - \mu^2 I_{13})^{-1}, \tag{33b}$$

where ρ is chosen slightly greater than 1 in order to have $\det(\Psi^{-1}) \neq 0$ and $\lambda_{\max}(ZX)$ is the maximal eigenvalue of the symmetric matrix ZX. In this paper $\rho = 1.01$.

In order to implement a minimal state-space realization of controller $\mathcal{K}(s)$ in (23), it suffices to check if some pole/zero simplifications appear in

$$\widetilde{K}(s) = W_1(s)K(s). \tag{34}$$

$W_2(s)$ do not appear in (34) since the integrator in $W_2(s)$ cannot be simplified because $K(s)$ internally stabilizes $G_s(s)$.

Since the system $G_s(s)$ is of order 13 (10 for $G(s)$ + 2 for $W_1(s)$ + 1 for $W_2(s)$), the designed controller $K(s)$ in (31) has the same order as $G_s(s)$. The order of $\widetilde{K}(s)$ is equal to 15 (13 for $K(s)$ + 2 for $W_1(s)$). After pole/zero simplifications procedure applied on $\widetilde{K}(s)$ in (34), 6 states are cancelled. So, the full-order controller $\overline{K}(s)$ with minimal state-space realization considered in this paper has 9 states and is expressed by

$$\overline{K}(s) = \begin{bmatrix} \overline{K}_i(s) & \overline{K}_{p_i}(s) & \overline{K}_{p_v}(s) \end{bmatrix}, \tag{35}$$

where the transfer functions of the controller $\overline{K}_i(s)$, $\overline{K}_{p_i}(s)$ and $\overline{K}_{p_v}(s)$ are given in (36).

$$\overline{K}_i(s) = \frac{-3.037.10^{-7}s^8 + 0.00111s^7 + 76.09s^6 + 7030s^5 + 1.941.10^5 s^4 + 1.742.10^6 s^3 + 5.152.10^6 s^2 + 3.372.10^6 s + 3.37.10^5}{s^9 + 295.3s^8 + 2.841.10^4 s^7 + 1.161.10^6 s^6 + 2.042.10^7 s^5 + 1.308.10^8 s^4 + 3.383.10^8 s^3 + 3.755.10^8 s^2 + 1.582.10^8 s + 1.416.10^7}, \tag{36a}$$

$$\overline{K}_{p_i}(s) = \frac{-6.227.10^{-7}s^8 + 0.002273s^7 + 155.6s^6 + 1.407.10^4 s^5 + 3.646.10^5 s^4 + 2.676.10^6 s^3 + 6.361.10^6 s^2 + 3.853.10^6 s + 3.763.10^5}{s^9 + 295.3s^8 + 2.841.10^4 s^7 + 1.161.10^6 s^6 + 2.042.10^7 s^5 + 1.308.10^8 s^4 + 3.383.10^8 s^3 + 3.755.10^8 s^2 + 1.582.10^8 s + 1.416.10^7}, \tag{36b}$$

$$\overline{K}_{p_v}(s) = \frac{-6.622.10^{-8}s^8 + 0.0002418s^7 + 16.56s^6 + 1500s^5 + 3.933.10^4 s^4 + 3.022.10^5 s^3 + 7.598.10^5 s^2 + 4.698.10^5 s + 4.609.10^4}{s^9 + 295.3s^8 + 2.841.10^4 s^7 + 1.161.10^6 s^6 + 2.042.10^7 s^5 + 1.308.10^8 s^4 + 3.383.10^8 s^3 + 3.755.10^8 s^2 + 1.582.10^8 s + 1.416.10^7}. \tag{36c}$$

The 2-DOF final full-order controller to be implemented $\mathcal{K}(s)$ defined in (23) is replaced by

$$\begin{aligned}\mathcal{K}(s) &= \overline{K}(s)W_2(s)\\ &= \left[\left(\frac{\overline{K}_i(s)}{s} + \overline{K}_{p_i}(s)\right) \quad \overline{K}_{p_v}(s)\right]\\ &= \left[\mathcal{K}_i(s) \quad \mathcal{K}_v(s)\right]\end{aligned} \tag{37}$$

and the control law u in Fig. 11 has the following expression in Laplace transform

$$U(s) = \mathcal{K}_i(s)(R(s) - \widetilde{I}(s)) + \mathcal{K}_{p_v}(s)\widehat{V}(s) \tag{38}$$

where $\widetilde{I}(s)$, $\widehat{V}(s)$ and $R(s)$ are the Laplace transforms of signals $\widetilde{i}, \widehat{v}$ and r, respectively.

The design specifications given in Section 4.1 are ensured by the designed controller since the singular values of $\overline{K}(s)W_2(s)G(s)$ are very close to the magnitude of $G_s(s)$ in Fig. 12.

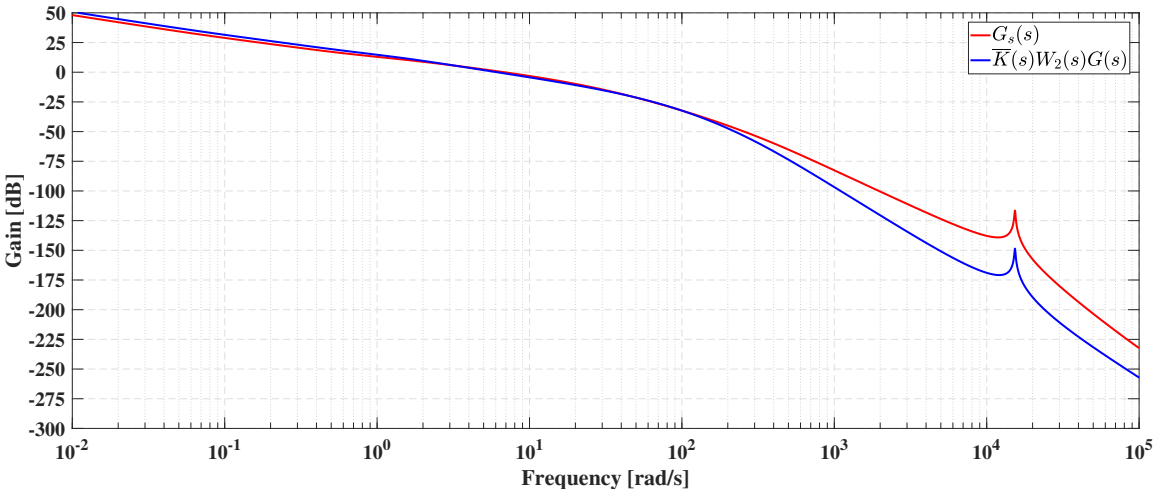

Figure 12: Frequency singular values of $G_s(s)$ and $\overline{K}(s)W_2(s)G(s)$

4.1.3. Robustness Analysis for Full-Order Controller

As mentioned in Remark 2, the criterion $b(G(s), \mathcal{K}(s))$ cannot be used to evaluate the robustness of the control law since

$$b(G(s), \mathcal{K}(s)) = b(G(s), W_2(s)K(s)W_1(s)) = 0.0022581 \tag{39}$$

while

$$b(G_s(s), K(s)) = \frac{1}{\mu} = 0.59699 \tag{40}$$

where $\mathcal{K}(s)$ is given in (37) and $K(s)$ is given in (31).

As pointed before Remark 2, these results are in adequation with the $\mathcal{H}_\infty$ norm of the sensibility function defined by the product of the sensibility function at the output by the process as shown below

$$\left\|(I + G(s)\mathcal{K}(s))^{-1}G(s)\right\|_\infty = 442.85, \tag{41a}$$

$$\left\|(I + G(s)W_2(s)K(s)W_1(s))^{-1}G(s)\right\|_\infty = 442.85, \tag{41b}$$

$$\left\|(I + G_s(s)K(s))^{-1}G_s(s)\right\|_\infty = 0.89021. \tag{41c}$$

Equations (39), (41a) and (41b) show that the pole/zero cancellations have no influence on the obtained robustness.

The obtained modulus margin defined in Remark 2 for the three controllers $K(s)$ in (31), $W_2(s)K(s)W_1(s)$ and $\mathcal{K}(s)$ in (37) is given by

$$\overline{b}(G_s(s), K(s)) = \overline{b}(G(s), W_2(s)K(s)W_1(s)) = \overline{b}(G(s), \mathcal{K}(s)) = 0.88224, \tag{42}$$

and confirms that the controllers provide a high level of robustness.

The next subsection is dedicated to the reduction of the order of the obtained controller. To preserve the structure of the implemented control law in (38) (i.e. the 2-DOF structure with integral action on the current, which is described in the transfer function $W_2(s)$), the truncation procedure must concern the 9-order controller $\overline{K}(s)$ given in (35) instead of the 10-order implemented controller $\mathcal{K}(s)$ given in (37).

4.2. Balanced Truncation of the NRCF of $\overline{K}(s)$ with Closed-Loop Considerations

4.2.1. Reduced-Order Controller Design

Reducing the order of the obtained controller $\overline{K}(s)$ given in (35) is a key step in the design procedure since the synthesis method in Section 4.1 results in a controller with a large order due to the fact that the order of the weighting $W_1(s)$ intervenes twice: first in the order of the shaped plant $G_s(s)$ in (22) (with weighting $W_2(s)$) and then in the order of $\overline{K}(s)$ itself in (35).

The balanced order truncation method developed in [47] has been extended to NLCF and NRCF (Normalized Right Coprime Factorization) in [5, 48, 49]. In [50] and [51], it is pointed out that the order truncation procedure proposed in [47] and [49] treats the controller to be reduced as an independent filter without considering the closed-loop environment and that closed-loop stability and performance consideration should be included in the balanced order truncation procedure applied to the full-order controller. Using the balanced frequency-weighted order reduction developed by Enns in [52], one of the authors with co-workers proposed a balanced truncation of the of the full-order NRCF controller in [53] and [54] that takes into account closed-loop stability and performance using closed-loop

sensitivity functions as frequency weightings.

he truncation of controller $\overline{K}(s)$ is called $\overline{K}_{\overline{r}}(s)$, and $\overline{r}$ is the order of $\overline{K}_{\overline{r}}(s)$. It follows that the reduced-order version of the controller to be implemented $\mathcal{K}(s)$ given in (37) is called $\mathcal{K}_{\overline{r}}(s)$, and has an order equal to $\overline{r}+1$ due to the integrator in $W_2(s)$.

It is important to mention that this reduction method exists only in [53] and [54]: [53] is not available on `IEEE xplore` and is briefly detailed in [54] due to lack of place. Moreover, to date, this reduction method has not been applied on an experimental test bench. Therefore, the balanced frequency weighting truncation of the controller's NRCF of $\overline{K}(s)$ presented in [53] and [54] is detailed in seven steps as follows:

a) Calculate the state-space realization of the controller $\overline{K}(s)$ defined in (35): $\overline{K}(s) = \overline{C}(sI_9 - \overline{A})^{-1}\overline{B}$.

b) Compute the NRCF of $\overline{K}(s)$ given by

$$\overline{K}(s) = Q(s)P^{-1}(s), \tag{43}$$

where $Q(s) \in \mathcal{H}_\infty$ and $P(s) \in \mathcal{H}_\infty$ satisfy

$$P^T(-s)P(s) + Q^T(-s)Q(s) = I_3 \quad \forall\, s \in \mathbb{C}.$$

Calculating the solution $\overline{X}$ of the following Riccati algebraic equation

$$0 = \overline{A}^T\overline{X} + \overline{X}\,\overline{A} - \overline{X}\,\overline{B}\,\overline{B}^T\overline{X} + \overline{C}^T\overline{C}, \tag{44}$$

we obtain the following NRCF of $\overline{K}(s)$ [1]

$$\begin{bmatrix} Q(s) \\ P(s) \end{bmatrix} = \left[\begin{array}{c|c} \widehat{A} & \widehat{B} \\ \hline \widehat{C}_Q & 0 \\ \widehat{C}_P & I_3 \end{array}\right] = \left[\begin{array}{c|c} \overline{A} - \overline{B}\,\overline{B}^T\overline{X} & \overline{B} \\ \hline \overline{C} & 0 \\ -\overline{B}^T\overline{X} & I_3 \end{array}\right]. \tag{45}$$

[1] $\left[\begin{array}{c|c} A & B \\ \hline C & D \end{array}\right] = C\,(sI - A)^{-1}\,B + D$ as in [4, 5].

c) Calculate a minimal state-space realization (A_o, B_o, C_o, D_o) of the following frequency weighting $W_o(s)$

$$\begin{aligned} W_o(s) &= -\left(\begin{bmatrix} -P^{-1}(s) & 0 \end{bmatrix} - P^{-1}(s)(I_3 + G_a(s)\overline{K}(s))^{-1} \right. \\ &\qquad \left. \times G_a(s)\begin{bmatrix} -\overline{K}(s) & I_3 \end{bmatrix}\right) \\ &= P(s)^{-1}\left(I_3 + G_a(s)\overline{K}(s)\right)^{-1}\begin{bmatrix} G_a(s) & I_3 \end{bmatrix} \\ &= C_o(sI - A_o)^{-1}B_o + D_o \end{aligned} \tag{46}$$

where $P(s)$ is given in (43) and $G_a(s)$ is the augmented plant defined as follows

$$G_a(s) = W_2(s)G(s) \tag{47}$$

d) As explained in [52], the weighted observability Gramian Σ_o and the controllability Gramian Σ_c are obtained using the following procedure:

i) Compute matrices A_f, B_f and C_f given by

$$A_f = \begin{bmatrix} \widehat{A} & 0 \\ B_o\widehat{C} & A_o \end{bmatrix}, B_f = \begin{bmatrix} I_8 \\ 0 \end{bmatrix}, C_f = \begin{bmatrix} D_o\widehat{C} & C_o \end{bmatrix} \tag{48}$$

with $\widehat{C}^T = \begin{bmatrix} \widehat{C}_Q^T & \widehat{C}_P^T \end{bmatrix}$ and where $\widehat{A}$, $\widehat{C}_P$ and $\widehat{C}_Q$ are given in (45). Notice that

$$W_o(s)\begin{bmatrix} Q(s) \\ P(s) \end{bmatrix} = C_f(sI - A_f)^{-1}B_f.$$

ii) Solving the two following Lyapunov equations

$$0 = A_f^T\Sigma_{fo} + \Sigma_{fo}A_f + C_f^TC_f \tag{49a}$$

$$0 = \widehat{A}\Sigma_c + \Sigma_c\widehat{A}^T + \widehat{B}\widehat{B}^T \tag{49b}$$

provides the weighted observability Gramian Σ_o and the controllability Gramian Σ_c where

$$\Sigma_o = B_f^T\Sigma_{fo}B_f. \tag{50}$$

e) Let T be the balancing transformation that diagonalized the product $\Sigma_c\Sigma_o$ and the diagonal balanced Gramian

Σ_b is given by

$$\Sigma_b = T^{-1}\Sigma_c\Sigma_o T \tag{51}$$

with Hankel singular values sorted in descending order and the frequency weighted balanced state-space realization of the NRCF of $\overline{K}(s)$ is given by

$$\begin{bmatrix} Q(s) \\ P(s) \end{bmatrix} = \left[\begin{array}{c|c} \widetilde{A} & \widetilde{B} \\ \hline \widetilde{C}_Q & 0 \\ \widetilde{C}_P & I_3 \end{array}\right] = \left[\begin{array}{c|c} T^{-1}\widehat{A}T & T^{-1}\widehat{B} \\ \hline \widehat{C}_Q T & 0 \\ \widehat{C}_P T & I_3 \end{array}\right]. \tag{52}$$

f) Consider $\bar{r} < 9$ as the order of the balanced truncation. The frequency weighted truncated NRCF has the following state-space realization

$$\begin{bmatrix} Q_{\bar{r}}(s) \\ P_{\bar{r}}(s) \end{bmatrix} = \begin{bmatrix} \widetilde{C}_{Q_{\bar{r}}} \\ \widetilde{C}_{P_{\bar{r}}} \end{bmatrix} \left(sI_{\bar{r}} - \widetilde{A}_{\bar{r}}\right)^{-1} \widetilde{B}_{\bar{r}} + \begin{bmatrix} 0 \\ I_3 \end{bmatrix} \tag{53}$$

where matrices $\widetilde{A}_{\bar{r}}$, $\widetilde{B}_{\bar{r}}$, $\widetilde{C}_{Q_{\bar{r}}}$ and $\widetilde{C}_{P_{\bar{r}}}$ are composed by the block $(1 \ldots \bar{r} \times 1 \ldots \bar{r})$ of $\widetilde{A}$, the block $(1 \ldots \bar{r} \times 1 \ldots 3)$ of $\widetilde{B}$, the block $(1 \ldots 3 \times 1 \ldots \bar{r})$ of $\widetilde{C}_Q$ and the block $(1 \times 1 \ldots \bar{r})$ of $\widetilde{C}_P$, respectively.

g) The reduced order controller $\overline{K}_{\bar{r}}(s)$ is given by

$$\begin{aligned} \overline{K}_{\bar{r}}(s) &= \left[\begin{array}{c|c} \widetilde{A}_{\bar{r}} - \widetilde{B}_{\bar{r}}\widetilde{C}_{P_{\bar{r}}} & \widetilde{B}_{\bar{r}} \\ \hline \widetilde{C}_{Q_{\bar{r}}} & 0 \end{array}\right] \\ &= \begin{bmatrix} \overline{K}_{\bar{r}_i}(s) & \overline{K}_{\bar{r}_{p_i}(s)} & \overline{K}_{\bar{r}_{p_v}(s)} \end{bmatrix}, \end{aligned} \tag{54}$$

and the reduced controller $\mathcal{K}_{\bar{r}}(s)$ to be implemented is expressed as

$$\begin{aligned} \mathcal{K}_{\bar{r}}(s) &= \overline{K}_{\bar{r}}(s)W_2(s) \\ &= \begin{bmatrix} \left(\dfrac{\overline{K}_{\bar{r}_i}(s)}{s} + \overline{K}_{\bar{r}_{p_i}(s)}\right) & \overline{K}_{\bar{r}_{p_v}(s)} \end{bmatrix} \\ &= \begin{bmatrix} \left(\mathcal{K}_{\bar{r}_i}(s) + \mathcal{K}_{\bar{r}_{p_i}}(s)\right) & \mathcal{K}_{\bar{r}_{p_v}}(s) \end{bmatrix}. \end{aligned} \tag{55}$$

The closed-loop with negative feedback in Fig. 9 can be formulated as in Fig. 13 by replacing the full order

controller by the reduced-order controller $\overline{K}_{\bar{r}}(s)$

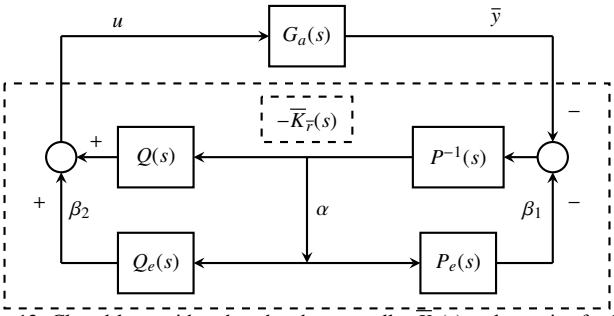

Figure 13: Closed-loop with reduced-order controller $\overline{K}_{\bar{r}}(s)$ and negative feedback

where

$$\begin{bmatrix} u \\ \alpha \end{bmatrix} = \begin{bmatrix} -\overline{K}(s) & -\overline{K}(s) & I_3 \\ -P^{-1}(s) & -P^{-1}(s) & 0 \end{bmatrix} \begin{bmatrix} \bar{y} \\ \beta_1 \\ \beta_2 \end{bmatrix}, \tag{56a}$$

$$\begin{bmatrix} \beta_1 \\ \beta_2 \end{bmatrix} = \begin{bmatrix} P_e(s) \\ Q_e(s) \end{bmatrix} \alpha. \tag{56b}$$

Therefore, Fig. 13 is identical to the following lower Linear Fractional Transformation (LFT) given in Fig. 14.

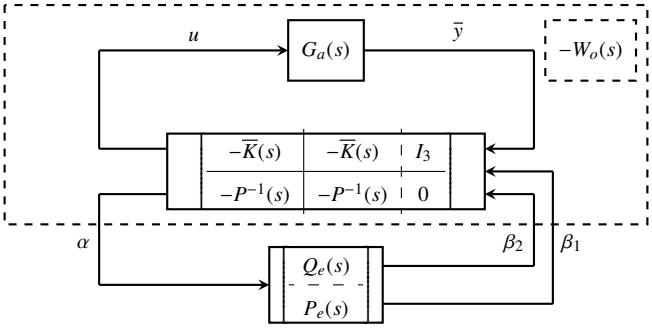

Figure 14: Closed-loop with reduced-order controller $\overline{K}_{\bar{r}}(s)$ and negative feedback

where $W_o(s)$ is an upper LFT given in (46).

So, using Fig. 14, the balanced frequency weighting truncation of the controller's NRCF of $\overline{K}(s)$ described below can be transformed into an $\mathcal{H}_\infty$ robust stability problem as shown in Theorem 1 and proven in [53] and [54].

Theorem 1. *[53], [54] The reduced-order controller $\mathcal{K}_{\bar{r}}(s)$ given in* (54)*, stabilizes internally the plant $G(s)$ if*

1. *the controller $\overline{K}(s)$ stabilizes internally the augmented plant $G_a(s)$,*

2. *the coprime factor errors* $Q_e(s) = Q_{\overline{r}}(s) - Q(s)$ *and* $P_e(s) = P_{\overline{r}}(s) - P(s)$ *are stable,*

3. *the inequality*

$$\left\| W_o(s) \begin{bmatrix} Q_{\overline{r}}(s) - Q(s) \\ P_{\overline{r}}(s) - P(s) \end{bmatrix} \right\|_\infty < 1 \tag{57}$$

is satisfied.

Remark 3. Since (see remark 5.3 of [4] and remark 4.9 of [5])

$$\|W_o(s)\|_\infty = \left\| \begin{bmatrix} I_3 \\ \overline{K}(s) \end{bmatrix} (I_3 + G_a(s)\overline{K}(s))^{-1} \begin{bmatrix} G_a(s) & I_3 \end{bmatrix} \right\|_\infty \tag{58}$$

the four sensitivity functions with full-order controller $\overline{K}(s)$ are close to the four sensitivity functions with the reduced-order controller $\mathcal{K}_{\overline{r}}(s)$. □

4.2.2. Evaluation of Reduced-Order Controller

Using Theorem 1 and Remark 3 the evaluation of the full and reduced order controllers is based on the following principle: the behavior of the reduced-order controller in closed loop must be close to that of the full-order controller. The evaluation of this proximity is performed with the four closed-loop sensitivity functions given in the transfer matrix $\mathcal{F}(s)$

$$\mathcal{F}(s) = \begin{bmatrix} \mathcal{K}(s) \\ I_2 \end{bmatrix} (I_2 + G(s)\mathcal{K}(s))^{-1} \begin{bmatrix} I_2 & G(s) \end{bmatrix} \tag{59}$$

for the full-order controller $\mathcal{K}(s)$ to be implemented given in (37). For the reduced-order controller $\mathcal{K}_{\overline{r}}(s)$ to be implemented, given in (55), the transfer matrix $\mathcal{F}(s)$ is replaced by $\mathcal{F}_{\overline{r}}$. This proximity is measured with the gap metric defined in (60): in proposition 1 in [55] and in equation 2 in [56], the gap metric between transfer functions $P_1(s)$ and $P_2(s)$, called $\delta(P_1(s), P_2(s))$, is given by

$$\begin{aligned} \delta(P_1(s), P_2(s)) = \max \Bigg\{ & \inf_{\Theta(s)\in\mathcal{H}_\infty} \left\| \begin{bmatrix} \overline{M}_1(s) \\ \overline{N}_1(s) \end{bmatrix} - \begin{bmatrix} \overline{M}_2(s) \\ \overline{N}_2(s) \end{bmatrix} \Theta(s) \right\|_\infty, \\ & \inf_{\Theta(s)\in\mathcal{H}_\infty} \left\| \begin{bmatrix} \overline{M}_2(s) \\ \overline{N}_2(s) \end{bmatrix} - \begin{bmatrix} \overline{M}_1(s) \\ \overline{N}_1(s) \end{bmatrix} \Theta(s) \right\|_\infty \Bigg\} \end{aligned} \tag{60}$$

where ($\overline{N}_1(s)$, $\overline{M}_1(s)$) and ($\overline{N}_2(s)$, $\overline{M}_2(s)$) are NRCF of $P_1(s)$ and $P_2(s)$, respectively.

The obtained gap metrics for closed-loop sensitivity functions are small and given in Table 3.

Table 3: Gap metric for the closed-loop sensitivity functions

Order $\overline{r}$	$\delta(\mathcal{F}(s), \mathcal{F}_{\overline{r}}(s))$
8	3.2172×10^{-5}
7	0.00035543
6	0.00093697
5	0.0010081
4	0.0018083
3	0.01148
2	0.040401
1	0.093676

In Table 3, the gap metric for reduced-order controllers $\mathcal{K}_1(s)$, $\mathcal{K}_2(s)$ and $\mathcal{K}_3(s)$ are higher than those of $\mathcal{K}_4(s)$ to $\mathcal{K}_8(s)$. Therefore, to analyze the effect of the reduction method on the closed-loop specifications, only the frequency singular values of $\mathcal{K}_1(s)G(s)$, $\mathcal{K}_2(s)G(s)$ and $\mathcal{K}_3(s)G(s)$ are plotted in Fig. 15.

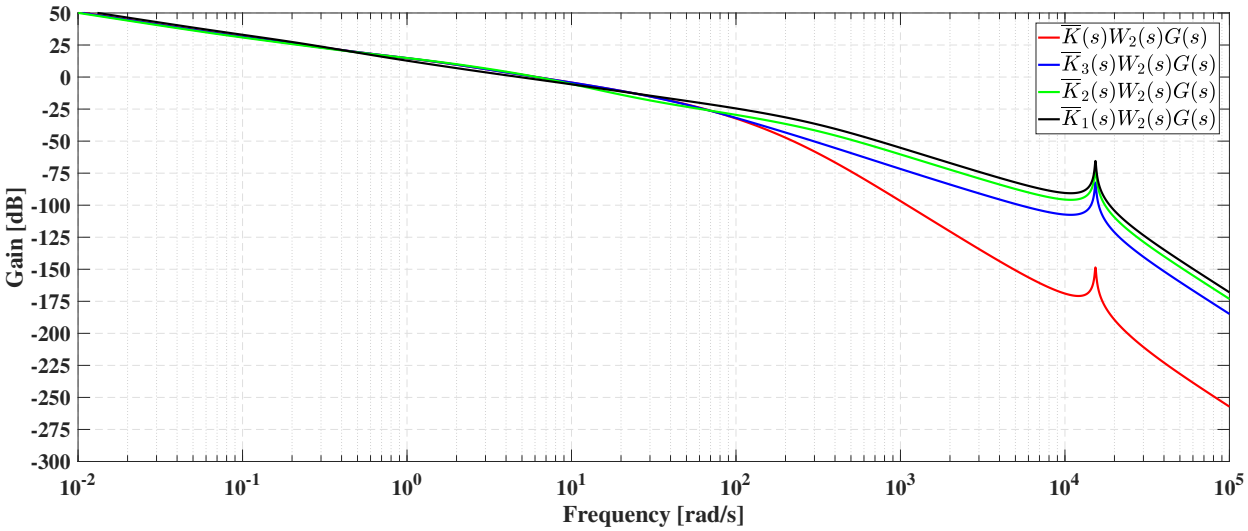

Figure 15: Frequency singular values of $\overline{K}(s)W_2(s)G(s)$, $\overline{K}_3(s)W_2(s)G(s)$, $\overline{K}_2(s)W_2(s)G(s)$ and $\overline{K}_1(s)W_2(s)G(s)$

In the frequency bandwidth (before 10^2 rad/s) the four curves are very close. The open-loop gain for full and reduced-order controllers differ after the frequency bandwidth. The $\mathcal{K}_3(s)$ curve shows better tracking of design specifications than those of $\mathcal{K}_2(s)$ and $\mathcal{K}_1(s)$, since its peak is lower. However, the obtained attenuation of the peak for the three reduced-order controllers is satisfactory since it is between -80 and -60 dB.

4.3. Robustness Analysis With Regards to Model Identification and RES Framework

In this section, the robustness of full- and reduced-order controllers are analyzed with regards to the five identified models in Sections 3.2 and 3.3 and to the variations of V_i provided by RES. By using the same approach as for identified model $F_{EIS_6}(s)$ in Section 3.3, the four other models $F_{EIS_5}(s)$, $F_{OE_1}(s)$, $F_{OE_2}(s)$ and $F_{OE_3}(s)$ are connected with the SIBC (see Fig. 8). For all obtained systems (identified models coupled with SIBC), the variations range of V_i considered in this paper is [25 V, 55 V].

The robustness is evaluated for each controller order $\bar{r}$, i.e. $\bar{r} = 15$ corresponds to controller $\widetilde{K}(s)$ before pole/zero cancellations given in (34), $\bar{r} = 9$ is associated to controller $\mathcal{K}(s)$ after pole/zero cancellations given in (37) and $\bar{r} = 8$ to $\bar{r} = 1$ stand for $\mathcal{K}_{\bar{r}}(s)$ given in (55). The used robustness criterion is modulus margin defined in Remark 2 and employed in (42).

Table 4: Modulus margins defined in Remark 2

Order $\bar{r}$	$V_i = 25$ V	$V_i = 40$ V	$V_i = 55$ V
15	[0.88936, 0.92289]	[0.84128, 0.88353]	[0.79845, 0.84735]
9	[0.88936, 0.92289]	[0.84128, 0.88353]	[0.79845, 0.84735]
8	[0.88935, 0.92291]	[0.84129, 0.88357]	[0.79849, 0.8474]
7	[0.88948, 0.92309]	[0.84166, 0.88378]	[0.79895, 0.84759]
6	[0.88976, 0.92307]	[0.8418, 0.88364]	[0.7989, 0.84734]
5	[0.88792, 0.92209]	[0.83927, 0.88286]	[0.79645, 0.84714]
4	[0.88787, 0.92203]	[0.83918, 0.88278]	[0.79633, 0.84703]
3	[0.88726, 0.92145]	[0.83812, 0.88193]	[0.79494, 0.84598]
2	[0.88223, 0.936]	[0.86775, 0.92863]	[0.86414, 0.92842]
1	[0.98829, 0.99073]	[0.98203, 0.98669]	[0.97611, 0.98204]

Due to lack of place only three value of V_i are presented in Table 4: the minimal value $V_i = 25$ V, the nominal value $V_i = 40$ V used for the design of the full- and reduced-order control laws, and the maximal value $V_i = 55$ V. Note that the modulus margins obtained for all variations in V_i are within the range of those provided by the minimum and maximum values of V_i. For each controller and each value of V_i, the interval between the minimum and maximum value of the module margin for the five considered systems is given.

The level of robustness with regards to V_i variations and each identified model is satisfactory since the modulus margin is always superior to 0.79494 0.79845. Therefore, large model parameter uncertainties can be tolerated by the designed full- and reduced-order controllers.

5. Experimental Validation

After describing the test bench, the controllers $\mathcal{K}(s)$ in (37) and $\mathcal{K}_{\bar{r}}(s)$ in (55) are evaluated in the following situations:

(1) for $V_i = 40\,\text{V}$, the tracking of the current reference is checked for several changes in operating points i (see Section 5.2);

(2) variations of V_i are considered to take into account the intermittence of RES in Section 5.3 in two cases: variations which emulate a wind turbine (Section 5.3.1) and abrupt variations (Section 5.3.2).

5.1. Test Bench Description

The test bench used for the validation of the designed controllers is shown in Fig. 16.

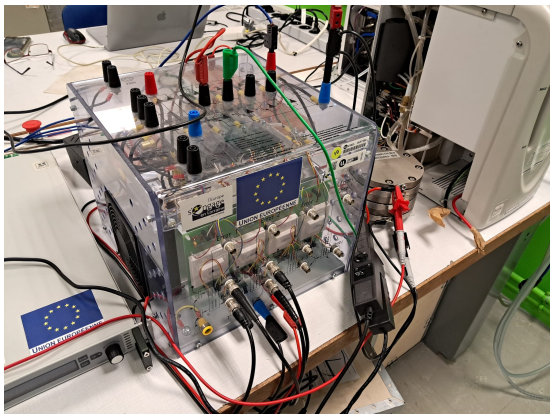

Figure 16: Test bench

The PEMWE stack specifications are given in Table 1, while the SIBC electrical components are given in the 1st paragraph of Section 3.3. A dSPACE DS1104 board is used for the acquisition of the stack current i and voltage v on the one hand, on the other hand to implement the control laws. The sampling time for data acquisition is $T_s = 0.001\,\text{s}$. The calculated control signals are sent to the PWM Matlab block to drive the power switches of the SIBC. An interface board converts 0-5 V PWM signals to 0-15 V signals required by the SEMIKRON driver boards SKHI 22. The frequency switching of the PWM is 10 kHz, i.e. $T_{\text{pwm}} = 5 \times 10^{-5}\,\text{s}$. The SIBC power supply is generated by a device called EA-PS 980-100 with a voltage value sent by the dSPACE DS1104 board. This emulates the intermittency of the RES through the voltage V_i.

5.2. Current Tracking With $V_i = 40\,V$

Since all reduced-order controllers are robust (see table 4), the three reduced-order controllers generating closed-loop behaviors furthest from full order (see table 3) are compared in Fig. 17, where full order corresponds to $\mathcal{K}(s)$ given in (37), reduced order corresponds to $\mathcal{K}_3(s)$, reduced order$_2$ and reduced order$_1$ correspond to $\mathcal{K}_2(s)$ and $\mathcal{K}_1(s)$, respectively. The $\mathcal{K}_3(s)$ controller meets the objective of the controller reduction method in section 4.2: to generate a closed-loop behavior close to that obtained with $\mathcal{K}(s)$. Indeed, the blue and red curves are almost identical in Fig. 17.

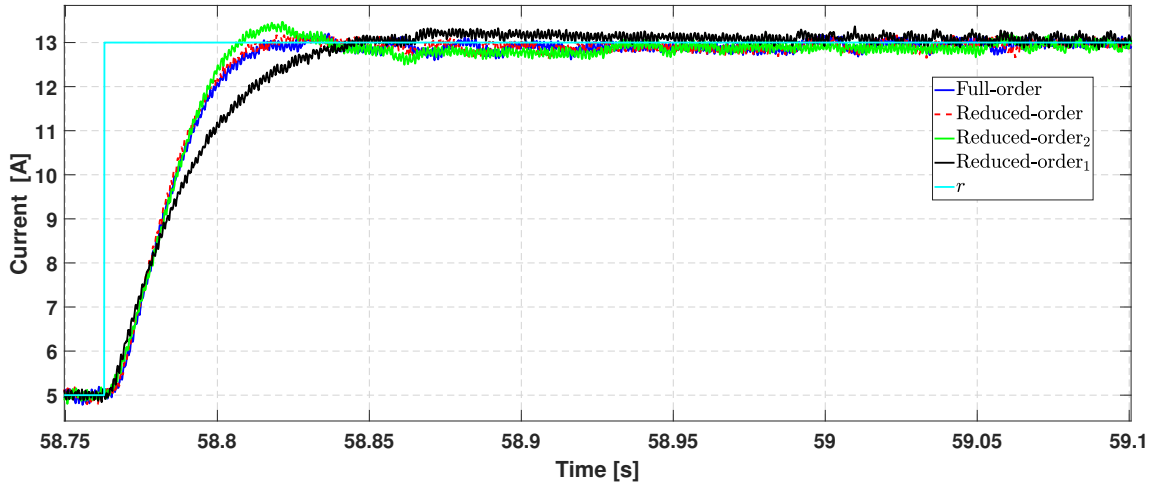

Figure 17: Current step responses for full and reduced-order controllers

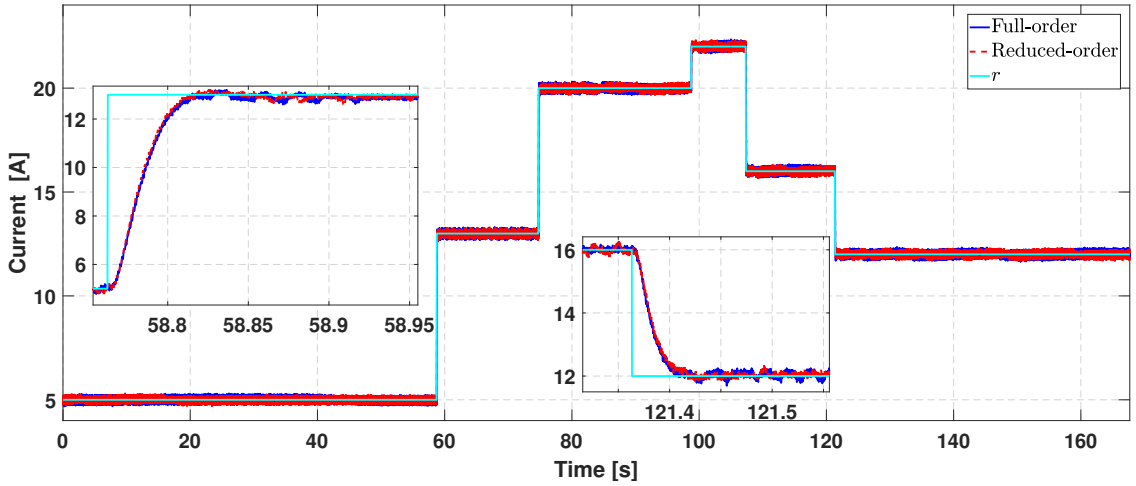

Figure 18: Operating current steps with zooms on increasing and decreasing steps: PEMWE current i response

It is not the case for $\mathcal{K}_2(s)$ and $\mathcal{K}_1(s)$: there is an overshoot for $\mathcal{K}_2(s)$ and the settling time for $\mathcal{K}_1(s)$ is too long. The analysis of Fig. 17 lead us to retained only $\mathcal{K}_3(s)$ for the sequel of Section 5.

The responses (5-22 A) in Fig. 18 and the associated zooms show that controllers $\mathcal{K}(s)$ and $\mathcal{K}_3(s)$ provide a very similar closed-loop behavior: the set-point is reached around 0.05 s without overshoot.

Fig. 19 shows the stack voltage for the step current changes applied for this scenario. Due to the non-linearities of the PEMWE and the fact that the voltage is not controlled, there is a difference between the voltage behaviors obtained with $\mathcal{K}(s)$ and $\mathcal{K}_3(s)$.

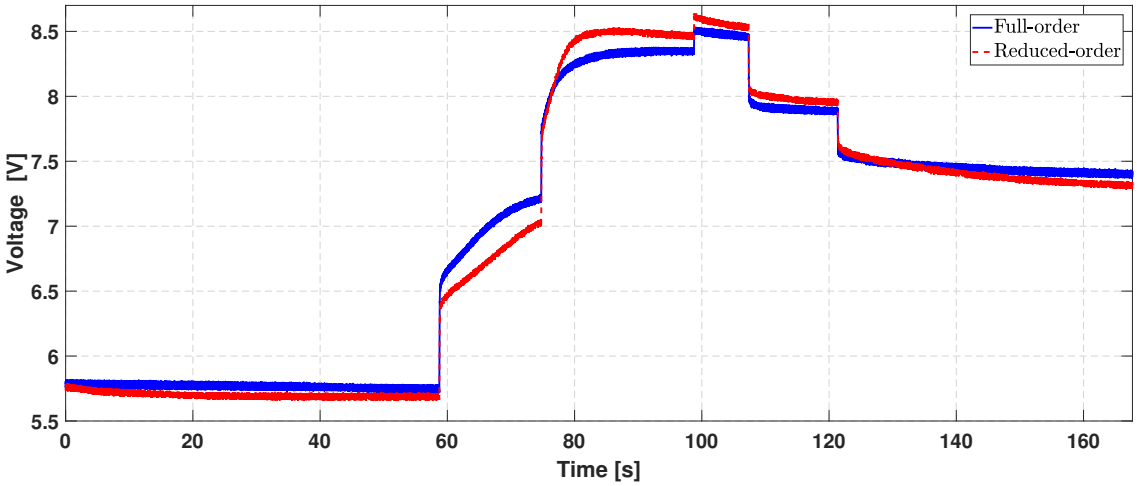

Figure 19: PEMWE voltage v response to current steps shown in Fig. 18

5.3. Intermittency of RES: V_i Variations

In this section, the robustness of full and reduced-order controllers is evaluated with regards to the intermittency of RES: V_i variations supplied by wind turbine in Section 5.3.1 and abrupt V_i variations in Section 5.3.2.

5.3.1. Variations of V_i Supplied by Wind Turbine

The emulated voltage V_i supplied by the wind turbine is given in Fig. 20 with a total duration of about 11.5 min. Two cases are considered: in the 1st case, the current is regulated at a fixed setpoint (18 A), and in the 2nd case, several setpoint changes are applied.

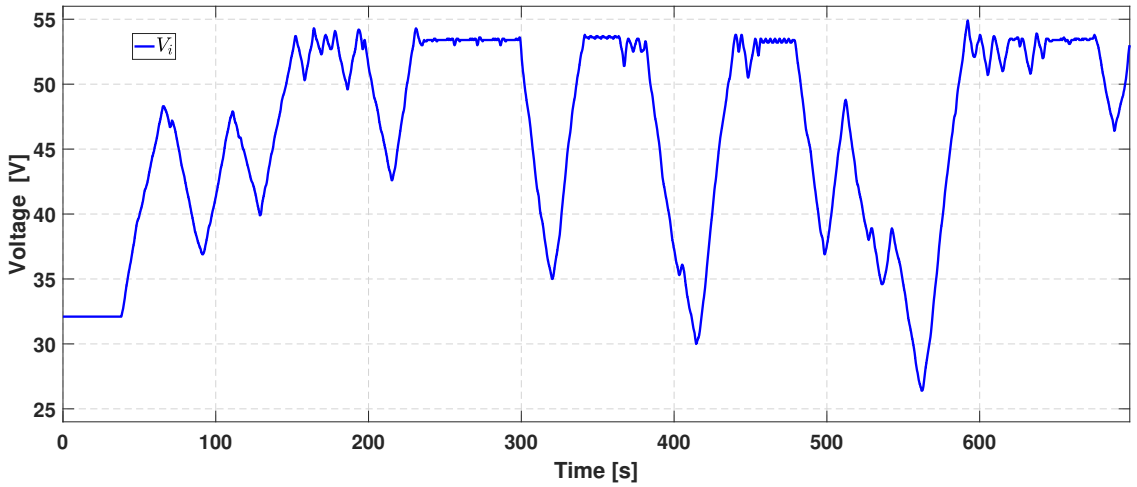

Figure 20: Variations of V_i supplied by wind turbine

In the 1st case, the large variations of V_i in Fig. 20 have almost no effects on the current i responses generated by $\mathcal{K}(s)$ and $\mathcal{K}_3(s)$ controllers as shown in Fig. 21. To illustrate this point, the large variations in V_i around 320 s, 420 s

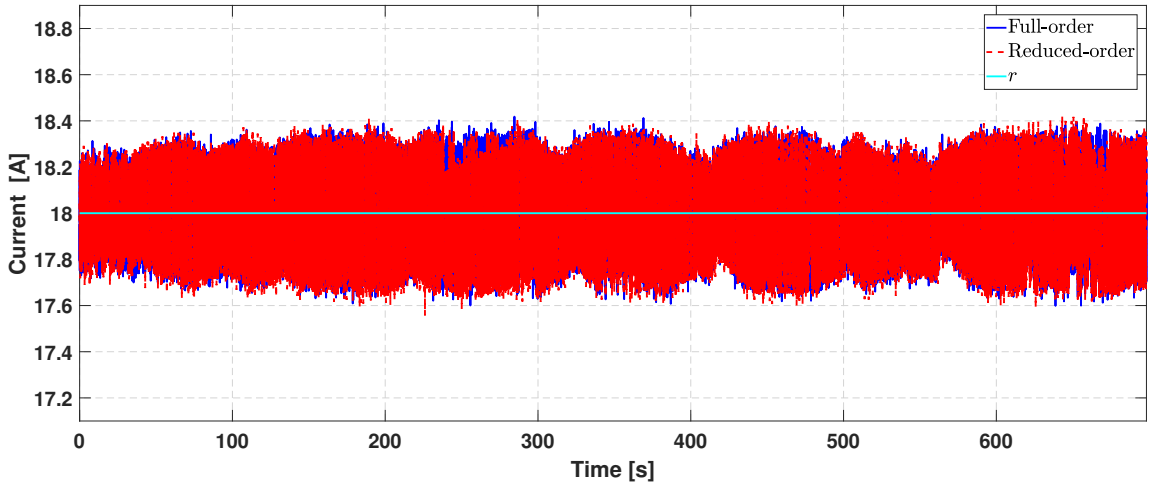

Figure 21: Current i responses due to variations of V_i in Fig. 20 without set-point change

and 570 s in Fig. 20 do not significantly affect the steady-state behavior of the closed-loop current responses i in the time intervals [280 s 340 s], [380 s 470 s] and [500 s 620 s] in Fig. 21, respectively.

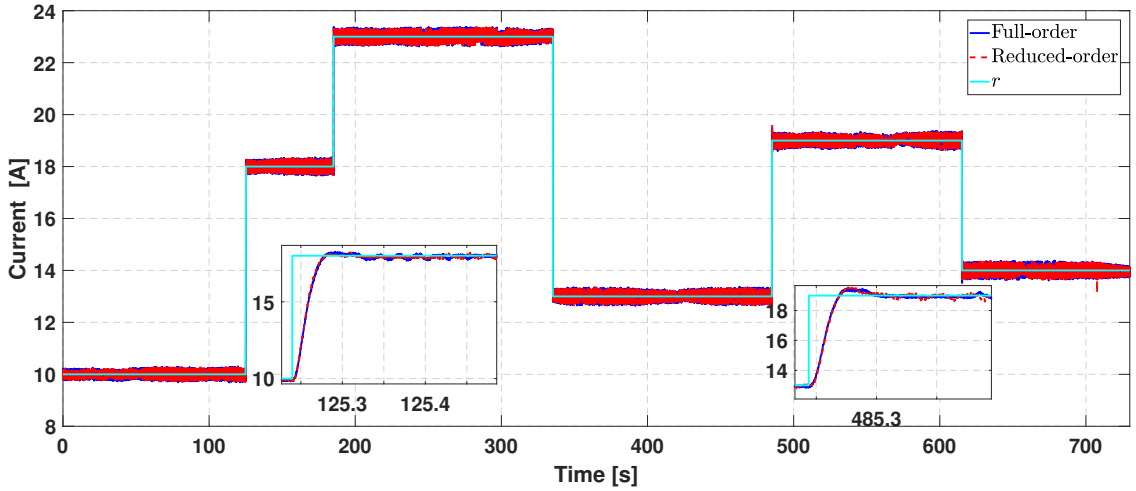

Figure 22: Current i responses due to variations of V_i in Fig. 20 with set-point changes

In the 2nd case, several changes on the desired current r when V_i is changing are made in order to evaluate the closed-loop with $\mathcal{K}(s)$ and $\mathcal{K}_3(s)$ controllers as shown in Fig. 22. The zooms in Fig. 22 and Fig. 23 show that both controllers guarantee that the desired current r is followed with slight overshoot and the settling time between 0.05 s and 0.07 s. For the two cases treated, both $\mathcal{K}(s)$ and $\mathcal{K}_3(s)$ controllers provide a similar closed-loop behavior as in Section 5.2.

The realistic variations in the voltage V_i supplied by a wind turbine have no significant effect on the regulated current i, i.e. the controllers $\mathcal{K}(s)$ and $\mathcal{K}_3(s)$ maintain the current at the desired value despite these realistic variations.

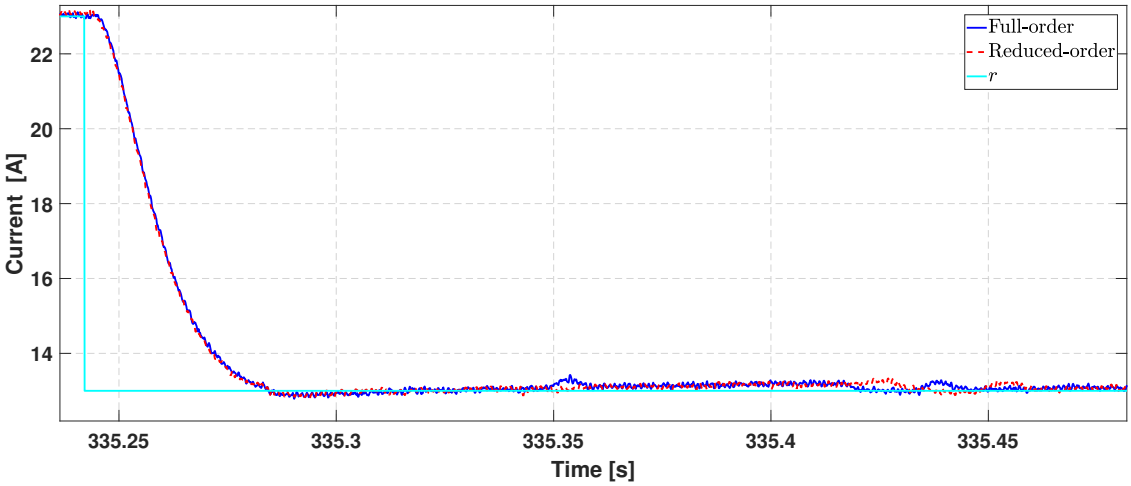

Figure 23: Zoom on Fig. 22

It should be noticed that the voltage variations V_i in Fig. 20 have a slower dynamic than the obtained closed-loop settling times. So, to study the effects of V_i variations on the closed-loop behaviors, it is interesting to generate more fast and abrupt changes in V_i. This is the aim of Section 5.3.2.

5.3.2. Abrupt Variations of Supplied Voltage V_i

The emulated voltage V_i with abrupt variations is given in Fig. 24 with a total duration around 7 min. As in Section 5.3.1, two cases are considered: in the 1st case, the current is regulated at a fixed setpoint (18 A), and in the 2nd case, several setpoint changes are applied.

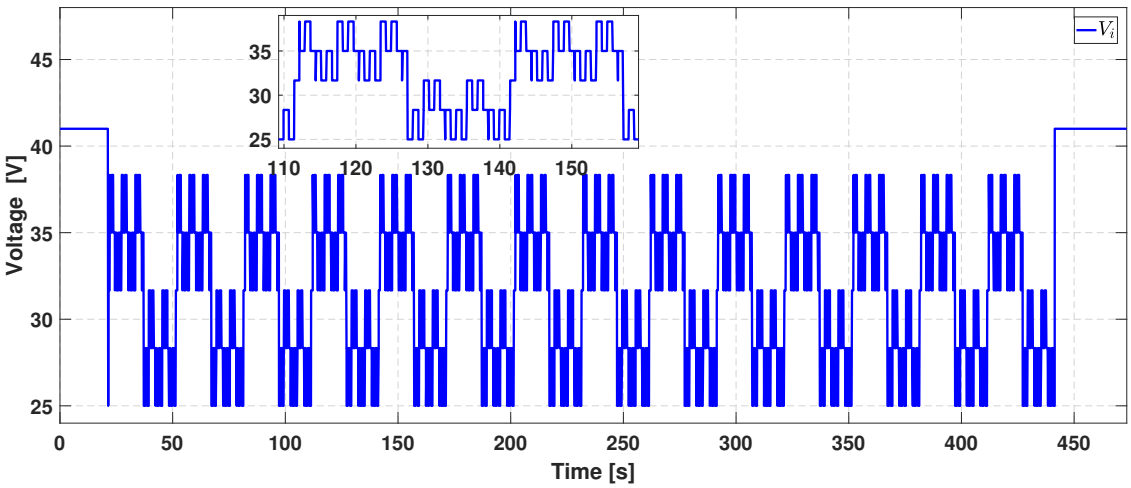

Figure 24: Abrupt variations of supplied RES voltage $V_i(t)$

In the 1st case, the abrupt variations in V_i in Fig. 24 have significant effects on the i current responses generated by the $\mathcal{K}(s)$ and $\mathcal{K}_3(s)$ controllers, as shown in Fig. 25, but these effects are quickly rejected. Indeed, for abrupt

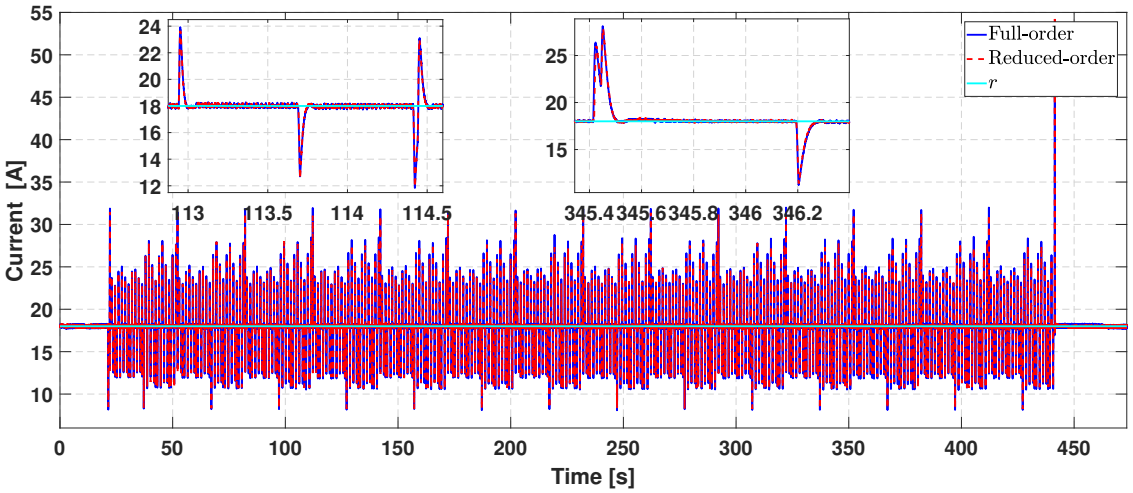

Figure 25: Current i responses due to variations of V_i in Fig. 24 without set-point change

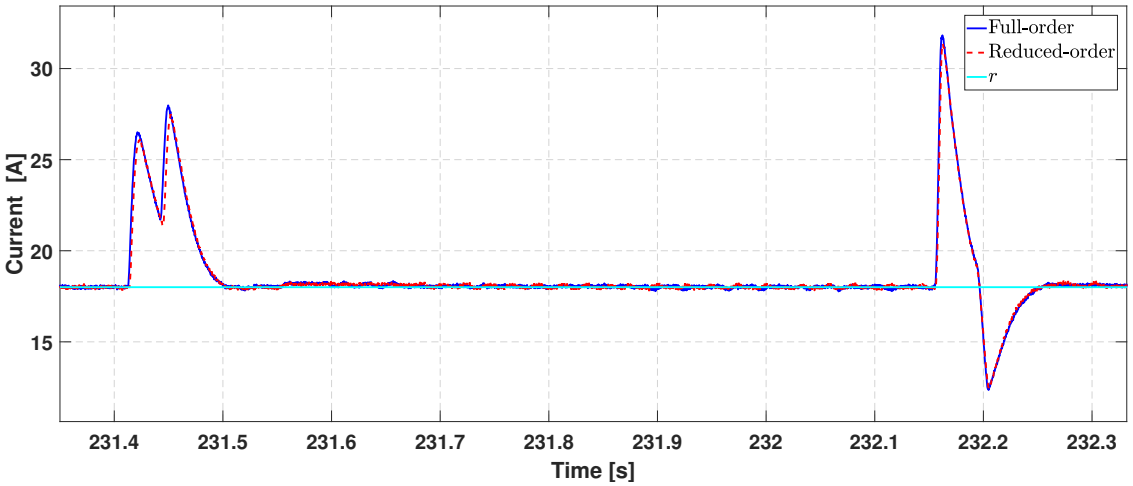

Figure 26: Zoom on Fig. 25

variations in V_i, the settling time to follow the desired current r is an interval between 0.015 s and 0.05 s as shown in the zooms of Fig. 25 and Fig. 26.

The 2nd case corresponds to Fig. 27 and Fig. 28. The same comments as in the 1st case can be made: when the current set-point changes, the effects of abrupt V_i variations are asymptotically rejected with settling time in an interval between 0.015 s and 0.05 s. In addition, for the two cases treated, both $\mathcal{K}(s)$ and $\mathcal{K}_3(s)$ controllers provide a similar closed-loop behavior as in Sections 5.2 and 5.3.1.

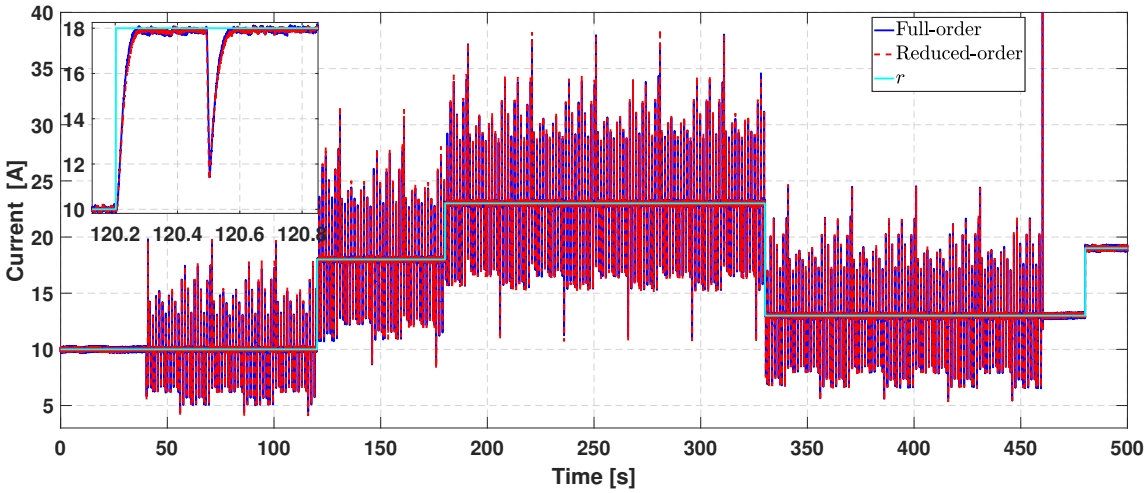

Figure 27: Current i responses due to variations of V_i in Fig. 24 with set-point changes

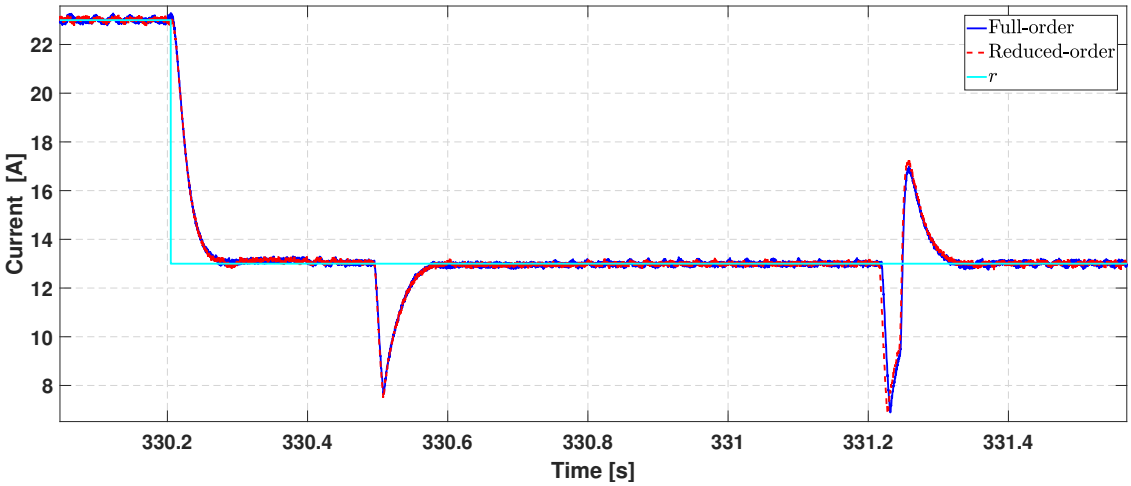

Figure 28: Zoom on Fig. 27

6. Discussion and conclusion

In this paper, a closed-loop framework based model and integrating RES intermittency via the variations of the supplied voltage has been proposed to DC/DC converter and PEM water electrolyzer. This closed-loop framework begins by modelling the entire system using several identification approaches, and continues by synthesizing a robust control law based on normalised coprime factorisations integrating a new closed-loop controller reduction approach. Several experimental validations are performed under RES variations with or without changes of the set-point. In order to highlight the link between the theoretical developments made in this paper (modelling, full-order control design and controller order reduction) and the experimental validations, a discussion in three parts is presented below.

(i) 1st part: PEMWE modelling and identification

- The PEMWE is a highly nonlinear system and can not be described by only one linear model in open-loop since its behavior is not the same at different operating points. The identification results reveal noticeable differences between the linear models obtained by EIS approach and OE method at the three operating points. This confirms that the PEMWE exhibits nonlinear behavior over its operating range, and that each model captures only local dynamics specific to its operating condition. The EIS approach allows the system to be excited over a wide range of frequencies, whereas the OE approach is applied to a smaller frequency range, despite the use of PRBS as the input signal. In addition, the use of a large amplitude in the PRBS contributes to accelerate PEMWE aging. For these reasons, the results obtained by EIS approach fits well with real data of the system than those generated by OE method.
- The fact that there are several operating points, and therefore several models that must be identified in open-loop, is treated as a control problem: it is the robustness of the controller that must guarantee performances and stability in closed-loop.

(ii) 2nd part: full-order controller design

- In order to guarantee this robustness and these performances in the face of parametric uncertainties due to the obtained identified model and V_i variations supplied by the RES, the control law synthesis method is based on two important points: choose an ad-hoc loop gain, called $G_s(s)$, by determining the weightings $W_1(s)$ and $W_2(s)$ and synthesize a control law that follows at best this loop gain by using an approach based on normalised coprime factorizations.
- This method allows the minimum inverse of the robust stability margin to be obtained analytically by solving two Riccati equations, whereas most methods in the literature rely on iterative approaches based on solving an LMI (Linear Matrix Inequality) feasibility problem. The obtained nominal modulus margin

(with $V_i = 40$ V and $F_{EIS_6}(s)$) is given in Eq. (42) and is equal to 0.88224. The modulus margin obtained with $V_i \in [\,25 \;\; 40\,]$ V and with five models identified in Section 3.2 is superior to 0.79845, see line $\bar{r} = 15$ in Table 4 . This theoritical results are in accordance with the experimental responses given in Section 5 : for all variations of V_i and of current set-points, the obtained settling-times are fast and overshoots are low.

- The developed controller has demonstrated a strong ability to track the current reference, i.e. to follow the desired hydrogen production, and maintain it even in the event of significant fluctuations in the supply voltage to the electrolysis system, see Section 5.3.2 . This enables efficient power-to-gas conversion by ensuring a rapid response in hydrogen production, within less than a second. This results in an optimal use of the energy supplied to the electrolyser.
- The drawback of the chosen controller design is that, due to the use of frequency weightings, the resulting full-order controller is higher: order of the system to be controlled plus two times weightings order, i.e. $10 + 2 \times 3 = 16$ in our case. Furthermore, determining the weighting $W_1(s)$ is not easy and requires the designer's expertise to translate robustness and performance specifications into the shaped loop gain.

(iii) 3rd part: controller order-reduction in closed-loop

- The reduction controller method developed has never been presented and explained in detail in the literature as in Section 4.2.1 . Furthermore, the article [53] describes this method very briefly, and the reference [54] is not available on `IEEE xplore`.
- The proposed controller truncation approach incorporates closed-loop behavior into the truncation process by using a frequency weight constituted by closed-loop sensitivity functions. As shown in Table 3 and in Section 5 , the closed-loop behaviors with the reduced-order controller $\mathcal{K}_3(s)$ closely approximate those obtained with the full-order controller $\mathcal{K}(s)$. We invite the reader to refer to supplementary material for additional experimental tests that have been carried out.
- The developed Theorem 1 gives sufficient condition to ensure closed-loop stability with the obtained reduced-order controller: the closed-loop stability is achieved for order $\bar{r} = 1, \ldots 8$ and validated experimentally.

An interesting perspective of this work is to consider that the intermittency of RES includes the following problem: the power supplied to the PEM electrolyzer may sometimes be too low to enable the desired hydrogen production.

The use of an energy storage system can contribute to stabilizing the power supply to the PEMWE. Such a energy storage system affects the overall cost of the plant and requires the development of an energy management strategy

between the PEM electrolyser, the storage system and energy from renewable sources. This issue is beyond the scope of this paper and will be the subject of future work.

References

[1] S. Sharshir, A. Joseph, M. Elsayad, A. Tareemi, A. Kandeal, M. Elkadeem, A review of recent advances in alkaline electrolyzer for green hydrogen production: performance improvement and applications, Int. J. of Hydrogen Energy 49 (2023) 458–488.

[2] D. Falcão, A. Pinto, A review on PEM electrolyzer modelling: guidelines for beginners, J. Cleaner Production 261 (2020) ID 121184.

[3] C. Li, J. Baek, The promise of hydrogen production from alkaline anion exchange membrane electrolyzers, Nano Energy 87 (2021) ID 106162.

[4] K. Glover, D. McFarlane, Robust stabilization of normalized coprime factor plant descriptions with $\mathcal{H}_\infty$-bounded uncertainty, IEEE Trans. Aut. Control 34 (1989) 821–830.

[5] D. McFarlane, K. Glover, Robust Controller Design Using Normalized Coprime Factor Plant Descriptions, Vol. 138 of Lecture Notes in Control and Information Sciences, Springer-Verlag, New York, 1990.

[6] D. McFarlane, K. Glover, A loop-shaping procedure using $\mathcal{H}_\infty$ synthesis, IEEE Trans. Aut. Control 37 (1992) 759–769.

[7] O. Atlam, M. Kolhe, Equivalent electrical model for a proton exchange membrane (PEM) electrolyser, Energy Conversion and Management 52 (2011) 2952–2957.

[8] M. Şahin, A photovoltaic powered electrolysis converter system with maximum power point tracking control, Int. J. of Hydrogen Energy 45 (2020) 9293–9304.

[9] Á.. Hernández-Gómez, V. Ramirez, D. Guilbert, B. Saldivar, Development of an adaptive static-dynamic electrical model based on input electrical energy for PEM water electrolysis, Int. J. of Hydrogen Energy 45 (2020) 18817–18830.

[10] F. da Costa Lopes, E. Watanabe, Experimental and theoretical development of a PEM electrolyzer model applied to energy storage systems, in: Proc. Brazilian Power Electronics Conf., Bonito-Mato Grosso do Sul, Brazil, 2009.

[11] X. Guo, S. Zhang, Z. Liu, L. Sun, Z. Lu, C. Hua, J. Guerrero, A new multi-mode fault-tolerant operation control strategy of multiphase stacked interleaved Buck converter for green hydrogen production, Int. J. of Hydrogen Energy 47 (2022) 30359–30370.

[12] M. Khalid Ratib, K. Muttaqi, M. Islam, D. Sutanto, A. Agalgaonkar, Electrical circuit modeling of proton exchange membrane electrolyzer: the state-of-the-art, current challenges, and recommendations, Int. J. of Hydrogen Energy 49 (2024) 625–645.

[13] A. Badoud, F. Merahi, B. Ould Bouamama, S. Mekhilef, Bond graph modeling, design and experimental validation of a photovoltaic/ fuel cell/ electrolyzer/ battery hybrid power system, Int. J. of Hydrogen Energy 46 (2021) 24011–24027.

[14] E. Nguyen, P. Olivier, M. Péra, E. Pahon, R. Roche, Impacts of intermittency on low-temperature electrolysis technologies: a comprehensive review, Int. J. of Hydrogen Energy 70 (2024) 474–492.

[15] K. Kang, C. Cao, C. Jiang, W. Li, C. Tang, Q. Liu, L. Huang, C. Wen, Capacity optimization for minimizing the cost on a hydrogen production system coupling the wind and solar power generation with pem water electrolysis, Energy (2025) 138076.

[16] N. Skordoulias, S. Karellas, D. V. Lyridis, S. G. Giannissi, G. Mitkidis, Res-electrolyser coupling within trieres hydrogen valley–a flexible technoeconomic assessment tool, Energy Conversion and Management 327 (2025) 119562.

[17] F. Lai, M. Wang, J. Zhou, J. Song, Y. Yuan, Hybrid pv-pv/t driven proton exchange membrane water electrolysis systems for hydrogen production: Experimental investigation and the role of thermal management, Energy Conversion and Management 344 (2025) 120326.

[18] R. Aguado, M. Tostado-Véliz, U. Desideri, F. Jurado, Optimizing proton exchange membrane electrolyzer performance through dynamic pressure and temperature control: A mixed-integer linear programming approach, Energy Conversion and Management 345 (2025) 120402.

[19] N. Franić, A. Z. Tomić, F. Barbir, I. Pivac, Machine learning two-step algorithm for prediction of proton exchange membrane water electrolyzer cell performance under variable power inputs, Energy conversion and management 343 (2025) 120229.

[20] L. Sánchez, D. Reigosa, A. Bilbao, I. Peña-Gonzalez, F. Briz, Comparative analysis of power converter topologies for hydrogen electrolyzers, IEEE J. of Emerging and Selected Topics in Power Electronics 12 (2024) 4325–4341.

[21] X. Guo, S. Zhang, F. Ding, J. Zhu, H. Bai, A novel DC-DC converter for electrolyzer with low ripple and high step down, IEEE Trans. Industrial ElectronicsHttps://doi.org/10.1109/TIE.2024.3355516 (2024).

[22] M. Koundi, H. El Fadil, A. Rachid, Z. El Idrissi, F. Giri, J. Guerrero, Output feedback sliding mode control of PEM EL-IBC system for hydrogen production, in: Proc. IFAC Int. Workshop on Adaptation and Learning in Control Systems, Winchester, UK, 2019.

[23] R. Zhou, F. Xiao, J. Liu, S. Duan, Y. Li, Modeling and control of a high-power DC-DC hydrogen converter based on DC grid, in: Proc. IEEE Asia Conf. on Power and Electrical Engineering, Shanghai, P.R. China, 2024.

[24] R. Maamouri, D. Guilbert, M. Zasadzinski, H. Rafaralahy, Proton exchange membrane water electrolysis: modeling for hydrogen flow rate control, Int. J. of Hydrogen Energy 46 (2021) 7676–7700.

[25] A. Garrigós, J. Lizán, J. Blanes, R. Gutiérrez, Combined maximum power point tracking and output current control for a photovoltaic-electrolyser DC/DC converter, Int. J. of Hydrogen Energy 39 (2014) 20907–20919.

[26] S. Dahbi, R. Aboutni, A. Aziz, N. Benazzi, M. Elhafyani, K. Kassmi, Optimised hydrogen production by a photovoltaic-electrolysis system DC/DC converter and water flow controller, Int. J. of Hydrogen Energy 41 (2016) 20858–20866.

[27] M. Şahin, H. Okumuş, M. Aydemiri, Implementation of an electrolysis system with DC/DC synchronous buck converter, Int. J. of Hydrogen Energy 39 (2014) 6802–6812.

[28] A. Kocalmis Bilhan, Integrated solar-based PEMWEs for green electricity production, Int. J. of Hydrogen Energy 75 (2024) 415–427.

[29] F. Alonge, S. Collura, F. D'Ippolito, D. Guilbert, M. Luna, G. Vitale, Design of a robust controller for DC/DC converter-electrolyzer systems supplied by μWECSs subject to highly fluctuating wind speed, Control Engineering Practice 98 (2020) ID 104383.

[30] B. Yodwong, D. Guilbert, M. Phattanasak, W. Kaewmanee, M. Hinaje, G.Vitale, Faraday's efficiency modeling of a proton exchange membrane electrolyzer based on experimental data, Energies 13 (2020) ID 4792.

[31] S. Nur Ozdemir, I. Taymaz, E. Okumuş, F. Gül Boyacı San, F. Akgün, Experimental investigation on performance evaluation of PEM electrolysis cell by using a Taguchi method, Fuel 344 (2023) ID 128021.

[32] T. Vidaković-Koch, T. Miličić, L. Živković, H. Seng Chan, U. Krewer, M. Petkovska, Nonlinear frequency response analysis: a recent review and perspectives, Current Opinion in Electrochemistry 30 (2021) ID 100851.

[33] T. Miličić, M. Sivasankaran, C. Blümner, A. Sorrentino, T. Vidaković-Koch, Pulsed electrolysis – explained, Faraday Discussions 246 (2023) 179–197.

[34] T. Miličić, K. Muthunayakage, T. Hoàng Vũ, T. Ritschel, L. Živković, T. Vidaković-Koch, The nonlinear frequency response method for the diagnosis of PEM water electrolyzer performance, Chemical Engineering J. 496 (2024) ID 153889.

[35] D. Brinker, N. Hensle, J. Horstmann de la Viña, I. Franzetti, L. Bühre, U. Andaluri, C. Menke, T. Smolinka, A. Weber, Inductive loops in impedance spectra of PEM water electrolyzers, J. of Power Sources 622 (2024) ID 235375.

[36] L. Ljung, System Identification: Theory for the User, Prentice Hall, Englewood Cliffs, New Jersey, 1987.

[37] T. Söderström, P. Stoica, System Identification, Prentice Hall, Englewood Cliffs, New Jersey, 1989.

[38] I. Landau, G. Zito, Digital Control Systems: Design, Identification and Implementation, Springer-Verlag, London, 2006.

[39] L. Ljung, System Identification Toolbox, User's Guide (2021).

[40] K. Ogata, Modern Control Engineering, Prentice Hall, Englewood Cliffs, New Jersey, 1970.

[41] J. Wibben, R. Harjanii, A high-efficiency DC-DC converter using 2 nH integrated inductors, IEEE J. of Solid-State Circuits 43 (2008)

844–854.

[42] R. Middlebrook, S. Cuk, A general unified approach to modelling switching-converter power stages, in: Proc. IEEE Power Electronics Specialists Conf., Cleveland, USA, 1976.

[43] N. Mohan, T. Undeland, W. Robbins, Power Electronics, 2nd Edition, Wiley, New York, 1995.

[44] B. Francis, A Course in $\mathcal{H}_\infty$ Control Theory, Vol. 88 of Lecture Notes in Control and Information Sciences, Springer-Verlag, New York, 1987.

[45] M. Vidyasagar, Control System Synthesis: A Factorization Approach, MIT Press, Cambridge, USA, 1985.

[46] M. Vidyasagar, Normalized coprime factorization for non-stricly proper systems, IEEE Trans. Aut. Control 33 (1988) 300–301.

[47] B. Moore, Principal component analysis in linear systems: controllability, observability, and model reduction, IEEE Trans. Aut. Control 26 (1981) 17–32.

[48] D. McFarlane, K. Glover, M. Vidyasagar, Reduced-order controller design using coprime factor model reduction, IEEE Trans. Aut. Control 35 (1990) 369–373.

[49] D. Meyer, Fractional balanced reduction: model reduction via fractional representation, IEEE Trans. Aut. Control 35 (1990) 1341–1345.

[50] B. Anderson, Y. Liu, Controller reduction: concepts and approaches, IEEE Trans. Aut. Control 34 (1989) 802–812.

[51] B. Anderson, Controller design: moving from theory to practice, IEEE Contr. Syst. Magazine 13 (4) (1993) 16–25.

[52] D. Enns, Model reduction with balanced realizations: an error bound and a frequency weighted generalization, in: Proc. IEEE Conf. Decision & Control, Las Vegas, USA, 1984.

[53] B. Frapard, M. Zasadzinski, L. Caramelle, M. Darouach, C. Champetier, $\mathcal{H}_\infty$ controller order reduction technique based on normalized coprime factors for space control systems on board implementation, in: Proc. European Contr. Conf., Rome, Italy, 1995.

[54] M. Zasadzinski, L. Caramelle, M. Darouach, B. Frapard, C. Champetier, Frequency weighted closed-loop balanced controller reduction using normalized coprime factor descriptions, in: Proc. IEEE American Control Conf., Seattle, USA, 1995.

[55] T. Georgiou, On the computation of the gap metric, Syst. & Contr. Letters 11 (1988) 253–257.

[56] T. Georgiou, M. Smith, Optimal robustness in the gap metric, IEEE Trans. Aut. Control 35 (1990) 673–686.